

EXPERIMENTAL FLOW MIXING EFFECTS IN THE COLD-LEG OF A PRESSURIZED  
WATER REACTOR FOR CFD-UQ

A Thesis

by

DANIEL OREA

Submitted to the Office of Graduate and Professional Studies of  
Texas A&M University  
in partial fulfillment of the requirements for the degree of  
MASTER OF SCIENCE

Chair of Committee,	Yassin A. Hassan
Co-Chair of Committee,	Rodolfo Vaghetto
Committee Member,	Maria King
Head of Department,	John E. Hurtado

May 2019

Major Subject: Nuclear Engineering

Copyright 2019 Daniel Orea

## ABSTRACT

The main objective of "Experimental Flow Mixing Effects in the Cold-Leg of a Pressurized Water Reactor for CFD-UQ" is to investigate mixing phenomena in the cold leg and of a Pressurized Water Reactor. The experimental facility constructed at Texas A&M collects high fidelity experimental data in a prototypical geometry to test uncertainty quantification methods. The purpose of gathering high-fidelity data is to validate computational fluid dynamic (CFD) codes.

Two different test conditions were incorporated for experiment. The "Open Test" utilized two working fluids with a density difference of approximately  $100 \text{ kg/m}^3$ . The "Blind Test" utilized two fluids that had a density difference of approximately  $200 \text{ kg/m}^3$ .

The open test results were produced for the purpose of being shared with the analyst for validation of the CFD model for the experiment. Both Open Test and Blind Test were conducted under isothermal conditions. Particle Image Velocimetry (PIV) and Laser Induced Fluorescence (LIF) methods were used in parallel to capture instantaneous velocity and fluid concentration measurements in an area within the cold leg near the vessel nozzle. PIV techniques were used to capture instantaneous velocity fields in the downcomer, which is the area directly below the nozzle. This data was temporally averaged to conduct a statistical analysis.

## DEDICATION

To my mother, my father, and my two brothers.

## ACKNOWLEDGMENTS

I would like to thank Dr. Yassin Hassan, Dr. Rodolfo Vaghetto, and Dr. Thien Nguyen for their guidance and support throughout the course of this research.

I would also like to thank all of the graduate and undergraduate students that participated in the experiment, with a special thanks to Vasileios Kyriakopoulos for spending countless hours conducting experiments.

## CONTRIBUTORS AND FUNDING SOURCES

### **Contributors**

This work was supported by a thesis committee consisting of Professors Yassin Hassan (Chair) and Rodolfo Vaghetto (Co-Chair) of the Department of Nuclear Engineering and Professor Maria King of the Department of Biological and Agricultural Engineering. All work for the thesis was completed by the student, under the advisement of Professors Yassin Hassan, Rodolfo Vaghetto, and Thien Nguyen of the Department of Nuclear Engineering.

### **Funding Sources**

Graduate study was supported by a graduate research assistant position in the Department of Nuclear Engineering at Texas A&M University.

## NOMENCLATURE

$\alpha$	Magnification Factor
BT	Blind Test
CFD	Computational Fluid Dynamics
CL	Cold Leg
$C_m$	Calculated Concentration
$C_0$	Known Concentration
D	Hydraulic Diameter
DC	Downcomer
$\delta U$	Flow Field Uncertainties Factors
ECCS	Emergency Core Cooling Systems
$\epsilon$	Relative Error
g	Acceleration due to Gravity
g'	Reduced Gravity Term
$H_H$	Height of Heavy Fluid
$H_L$	Height of Light Fluid
LIF	Laser Induced Fluorescence
LOCA	Loss of Coolant Accident
MIR	Matched Refractive index
RMS	Root Mean Square
OT	Open Test
PIV	Particle Image Velocimetry
PTS	Pressurized Thermal Shock

$\rho_H$	Density of Heavy Fluid
$\rho_L$	Density of Light Fluid
$\rho_{avg}$	Average Density
PWR	Pressurized Water Reactor
RPV	Reactor Pressure Vessel
$\sigma$	Variance
$\Delta t$	Time Interval of Successive Images
$U_H$	Heavy Fluid Front Velocity
$\Delta x$	Displacement of Particle

## TABLE OF CONTENTS

	Page
ABSTRACT .....	ii
DEDICATION .....	iii
ACKNOWLEDGMENTS .....	iv
CONTRIBUTORS AND FUNDING SOURCES .....	v
NOMENCLATURE .....	vi
TABLE OF CONTENTS .....	viii
LIST OF FIGURES .....	x
LIST OF TABLES.....	xii
1. INTRODUCTION AND LITERATURE REVIEW .....	1
2. OBJECTIVE AND SPECIFICATIONS.....	5
2.0.1 Objectives .....	5
3. EXPERIMENTAL FACILITY DESCRIPTION.....	7
4. TEST CONDITIONS AND MEASUREMENT LOCATIONS.....	11
4.1 Fluid Properties .....	11
4.2 Measurement Locations.....	14
5. EXPERIMENTAL METHODS AND MEASUREMENT TECHNIQUES .....	16
5.1 Particle Image Velocimetry .....	16
5.2 Laser Induced Fluorescence .....	17
5.2.1 LIF Calibration .....	18
5.3 Experimental Method .....	20
6. RESULTS AND ANALYSIS .....	25
6.1 Pressure Drop .....	25
6.2 Heavy Front Velocity .....	26
6.3 Open Test Velocity and Concentrations Results .....	27
6.3.1 Cold Leg PIV and LIF Results.....	28



6.3.2	Downcomer PIV Results .....	31
6.4	Blind Test Velocity and Concentrations Results .....	33
6.4.1	Cold Leg PIV and LIF Results.....	33
6.4.2	Downcomer PIV Results .....	35
7.	UNCERTAINTY ANALYSIS .....	38
7.0.1	PIV Uncertainty .....	38
7.0.2	LIF Error Sources .....	40
8.	CONCLUSION.....	44
	REFERENCES .....	46
	APPENDIX A. TAMU-PTSUQ-VOT-001-REV0 .....	50
	APPENDIX B. TAMU-PTSUQ-DWG-001-REV0 .....	60
	APPENDIX C. TAMU-PTSUQ-OCB-001-REV0 .....	69
	APPENDIX D. TAMU-PTSUQ-OT3-REV1.1.....	79
	APPENDIX E. TAMU-PTSUQ-BBC-001-REV2 .....	93

## LIST OF FIGURES

FIGURE	Page
2.1 Target Locations for Measurement of Velocity and Density Profiles. ....	6
3.1 Experimental Facility & Instrumentation. Blue solution represents the cold/heavier water. Yellow solution represents the hot/lighter water. ....	7
3.2 Vessel & Cold Leg Geometry. ....	8
3.3 Cold Leg Vessel Nozzle. ....	10
4.1 Density vs. Refractive Index of Solutions. ....	12
4.2 Viscosity of Fluids Mixtures. ....	13
4.3 Visualization Windows. ....	15
5.1 OT and BT LIF 5-Point Calibration Curve from Window Average Intensity. ....	19
5.2 OT LIF 5-Point Local Calibration Curve for a single point in point in space. ....	20
5.3 Camera Setup for Cold Leg Window. ....	22
5.4 a) Image without 552nm Light Filter. b) Image with 552nm Light Filter. ....	23
5.5 Camera System for Simultaneous PIV Measurements. ....	23
6.1 Pressure Difference across Valve. ....	26
6.2 Cold(Heavy) Fluid Front Velocity. ....	27
6.3 OT Cold Leg Time-Averaged Velocity Magnitude Contour. ....	28
6.4 OT Cold Leg Velocity Profiles Computed at CL1 for Various Temporal Durations. ..	29
6.5 OT Cold Leg LIF and PIV Results. ....	30
6.6 OT Cold Leg Concentration Profiles at CL1. ....	30
6.7 OT Downcomer Velocity Magnitude Contour. ....	31
6.8 OT Downcomer Velocity Magnitude Contour. ....	32

6.9	OT Downcomer Vertical Velocity Profiles Computed at DC1 for Various Temporal Durations.....	32
6.10	BT Cold Leg Time-Averaged Velocity Magnitude Contour.....	33
6.11	BT Cold Leg Velocity Profiles Computed at CL1 for Various Temporal Durations. ..	34
6.12	BT Cold Leg LIF and PIV Results. ....	34
6.13	BT Cold Leg Concentration Profiles at CL1. ....	35
6.14	OT Downcomer Velocity Magnitude Contour. ....	36
6.15	BT Downcomer Velocity Magnitude Contour. ....	36
6.16	BT Downcomer Vertical Velocity Profiles Computed at DC1 for Various Temporal Durations.....	37
7.1	Background Intensity Distribution.....	40
7.2	Normalized Intensity Along Horizontal Profile.....	41
7.3	Normalized Intensity Along vertical Profile. ....	42
8.1	End of Mixing. ....	44

## LIST OF TABLES

TABLE	Page
3.1 Dimensions of Vessels & Cold Leg.....	9
4.1 Fluid Properties of Sampled Mixtures (OT).....	12
4.2 OT and BT Fluid Properties.....	14
5.1 Equipment and Instrumentation Specification. ....	24
6.1 List of Test and Available Data. ....	25
7.1 Values Used for OT and BT Uncertainty Analysis. ....	39

## 1. INTRODUCTION AND LITERATURE REVIEW

The influence of density gradients on the dynamics of mixing fluids presents many challenges in turbulence research. There is a limited understanding of the underlying physics observed in mixing of fluids. These physical principles are non-trivial and there is a necessity for experimental data to improve and build upon existing computational models. Experimental measurement techniques that allow for the gathering of flow data are non-intrusive methods such as Particle Image Velocimetry (PIV) [1] and Laser Induced Fluorescence (LIF) [2]. These techniques allow for the acquirement of spatial and temporal velocity, temperature, or concentration measurements. However, in the presence of fluid mixing there can be density and/or temperature variations that directly affect the refractive index (RI). This poses a challenging problem when attempting to match the RI as it limits the fluid density differences. Past experiments have accomplished density differences of up 10% using a water-glycerol and 20% using water-salt solutions, however failed to match the index of refraction [3]. Having the ability to acquire large density differences under isothermal conditions is of great importance to which can be applied directly to numerical tools. Being able to to perform measurements at large density differences and acquiring spatial and temporal resolved results are of great importance. particularly the latter is essential to be applied directly to Computational Fluid Dynamics (CFD).

CFD is a well-established numerical tool that finds application to a multitude of diverse engineering disciplines. In nuclear engineering, the use of CFD is becoming widely popular in modeling situations in which coolant flow through complex geometries produces important multi-dimensional phenomena. For example, the mixing phenomena of hot and cold water, that take place in reactor accident scenarios. A Pressurized Thermal Shock (PTS) event is characterized by rapid cooling of the cold leg, downcomer and internal reactor pressure vessel (RPV) surface, due to the cold-water flooding. During emergency core cooling (ECC) situations, such as those after a LOCA, cold ECC water is injected into the hot water in the cold leg and downcomer. When the plumes of cold-water get in contact with the RPV wall, thermal stresses occur, which can be

dangerous for the vessel structure. To assess the severity of these stresses it is important to calculate the temperature distributions within the cold leg and the downcomer temperature gradients in time. Similarly, a PTS event poses a potentially significant challenge to the structural integrity of the cold leg pipe due to thermal fatigue and thermal shock. In a real process thermal stratification and wave formation inside the horizontal cold leg pipe can expose the pipe wall to periodic fluctuations of temperature and potentially result in fatigue cracking [4]. Understanding this phenomenon within the cold leg and downcomer is important to the safety of reactors and a crucial to the improvement of CFD codes.

The effect of density differences on thermal stratification is an important parameter for modeling areas susceptible to thermal fatigue. The temperature difference between the cold front propagating inside the horizontal cold leg pipe at the bottom and the hot water returning from the reactor vessel, produces large temperature gradients and local stresses, in addition to the mechanical loads present on the leg. As a result, thermal stratification accelerates thermal fatigue damages [5][6]. The mixing of the hot and cold coolant distribution in geometries is an important factor to consider during normal operation and in accident scenarios [7]. The study of fluid mixing for enhancing the safety of nuclear reactors is an ongoing subject of investigation, both experimentally and numerical methods to model these flow phenomena. In the future, these codes are expected to be used for assessing nuclear reactor safety of current and next generation IV reactor. This subject requires substantial validation from experiments, providing the necessary details of modeling of all structures important for fluid mixing [8].

There is also a direct application of the experimental data collected towards non-nuclear applications of CFD validation. Atmospheric fronts and ocean currents can be simulated as gravity driven flows induced by density fluctuations caused by temperature variations [9]. The Eddy formation within the cold leg of a PWR is a physical phenomenon that appears often in nature. The simulation of these Eddy's is a challenging problem that requires high fidelity data. The heat transfer problems related to non-isothermal mixing in pipes have caused concern and extensive research in the engineering community because of the thermal fatigue of pipe systems. Turbulent flow of

different velocity and density mix creating a contact interface between the fluids that oscillate because of hydrodynamic instabilities. This eventually leads to low-frequency oscillations with the pipe system potentially causing problems. The latter accelerate thermal-mechanical fatigue, damage the pipe structure and, ultimately, cause its failure [10].

The objective of the experiment is to go a step further in the application of single-phase CFD to nuclear safety issues with coolant mixing, possibly in presence of buoyancy effects. The OECD/NEA-Vattenfall T-Junction Benchmark investigated mixing with thermal fatigue phenomena [11]. MATiS-H benchmark investigated the flow in a 5x5 rod bundle behind a spacer grid with mixing devices [12]. The PANDA benchmark investigated the erosion of a light stratified layer, by a buoyant jet in a containment [13]. The GEMIX benchmark investigated mixing with density gradients, in the simple geometry of an isokinetic mixing layer and it was the first benchmark with application of uncertainty quantification [14]. In order to test uncertainty quantification methods in conditions closer to real reactor applications, it was decided to use data obtained in a more prototypical geometry, such as the one contracted at TAMU for the purposes of this study.

The experiment requires a preliminary validation of the CFD model. Open test (OT) results were produced for the purpose of being shared with the analyst before performing a blind test (BT). Non intrusive techniques such as PIV and LIF were utilized to produce these data sets. The experiments performed in the context of this exercise were isothermal because a temperature gradient would make it physically impossible for the refractive index (RI), which is a function of temperature, to match. The hot and cold water was simulated with surrogate solutions of selected physical and optical properties, with a similar approach adopted by [15][16][17][18]. The cold fluid is referred to as the heavy fluid and the hot fluid is referred to as the light fluid because of their respective densities. Focusing on variable densities and equal index of refraction in fluid mixing, all methods reported in scientific literature use two aqueous solutions. The two-aqueous solutions were able to reach density differences of 10% and 20%, while still maintaining a matched index of refraction. This study aims to collect high fidelity experimental data in the presence of mixing effects produced by density driven flow within the cold leg of the PWR. Experimental data

can be applied for CFD code validation and improve upon current models. This thesis describes the measurement techniques developed and applied, and the experimental results produced during the length of the experiment.



## 2. OBJECTIVE AND SPECIFICATIONS

Project outlines and specifications were outlined by Texas A&M based on the need for high-fidelity data to validate CFD codes.

### 2.0.1 Objectives

The main objective is to study density driven flow and the associated mixing phenomena in the cold leg and annular downcomer of a typical Pressurized Water Reactor (PWR) geometry. The purpose of gathering high-fidelity data is to validate computational fluid dynamic (CFD) codes.

The measurement techniques of Particle Image Velocimetry (PIV) and Laser Induced Fluorescence (LIF) will be applied to the cold leg and PIV will be used in the annular downcomer to produce velocity and concentration analysis. Since the flow is transient, it was not clearly defined over what period of time velocity and density can be temporally averaged or if simply instantaneous values may be used.

Data will be collected and analyzed to produce the following parameters of interest within the cold leg:

- Temporal evolution of the heavy fluid front position using cameras.
- Time averaged axial velocity profile in a vertical diameter of the pipe just upstream of conical section using PIV.
- Time averaged vertical velocity profile in a vertical diameter of the pipe just upstream of conical section using PIV.
- Velocity RMS fluctuation in a vertical profile of the pipe just upstream of conical section using PIV.
- Time averaged density (or salt concentration) profile in a vertical diameter of the pipe just upstream of conical section using LIF.

- Density RMS fluctuations a vertical profile of the pipe just upstream of conical section using LIF.

In the annular downcomer, since oscillations of the cold layer may occur, it may be useful to report instantaneous values of velocity. The following data will be collected and analyzed to produce the following parameters within the downcomer.

- Time averaged axial velocity profile in a vertical diameter of the annular downcomer just upstream of conical section using PIV.
- Time averaged vertical velocity profile in a vertical diameter of the annular downcomer just upstream of the conical section using PIV.
- Velocity RMS fluctuations in a horizontal profile of the annular downcomer just upstream of conical section using PIV

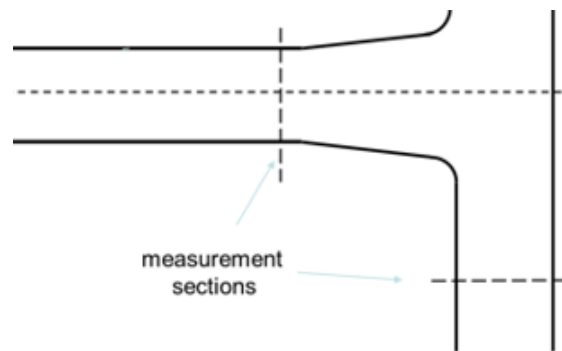


Figure 2.1: Target Locations for Measurement of Velocity and Density Profiles.

It is necessary to investigate repeat ability of each test to record sensitivity to boundary and initial conditions and to see possible unstable cold layer behavior in the downcomer. Each test will be conducted a minimum of three times. Results will be provided in a file format and distributed to benchmark participants.

### 3. EXPERIMENTAL FACILITY DESCRIPTION

The experimental test facility consists of two large transparent vessels connected through a horizontal acrylic pipe. One of the two vessels is designed to incorporate specific features and geometry of a typical reactor vessel. In particular the nozzle is constructed to realistically represent the fluid domain of the cold leg nozzle of a PWR vessel. An overview of the experimental facility with the instrumentation installed is provided in Figure 3.1.

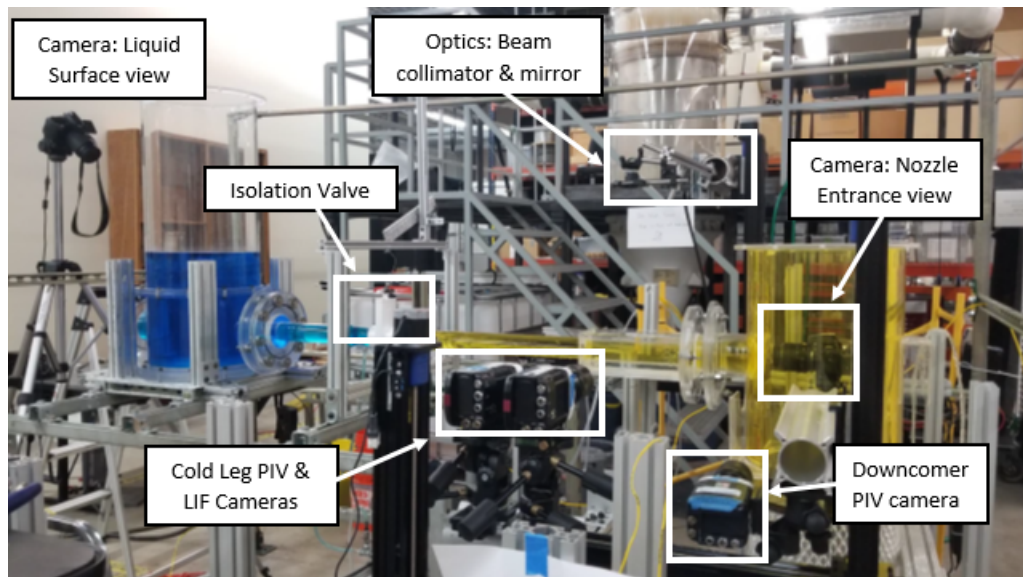


Figure 3.1: Experimental Facility & Instrumentation. Blue solution represents the cold/heavier water. Yellow solution represents the hot/lighter water.

The vessel on the left is used as reservoir for the solution simulating the cold/heavy water injection (blue solution in Figure 3.1), and is initially filled to a predetermined height. This vessel is referred to as the heavy vessel due to the heavier density fluid. The vessel on the right represents the reactor vessel. This is made by two acrylic cylinders, the external cylinder representing the vessel wall, and the internal cylinder representing the reactor barrel. The annular region between these cylinders represents the downcomer of the reactor, which is initially filled with a surrogate

solution to the hot water (yellow solution in Figure 3.1). This vessel is referred to as the light vessel because of the lower density fluid. An isolation valve is installed within the connecting horizontal leg to keep the two solutions isolated during test preparation. The isolation valve is attached to a spring lever mechanism to achieve consistent and repetitive opening times. A detailed explanation of the isolation valve opening time can be found in Appendix A. Attached to the valve is a switch that is used to trigger the cameras to begin recording when the isolation valve is open. Figure 3.2 and Table 3.1 provide the main dimensions of the heavy, light vessels and the leg that connect the two vessels.

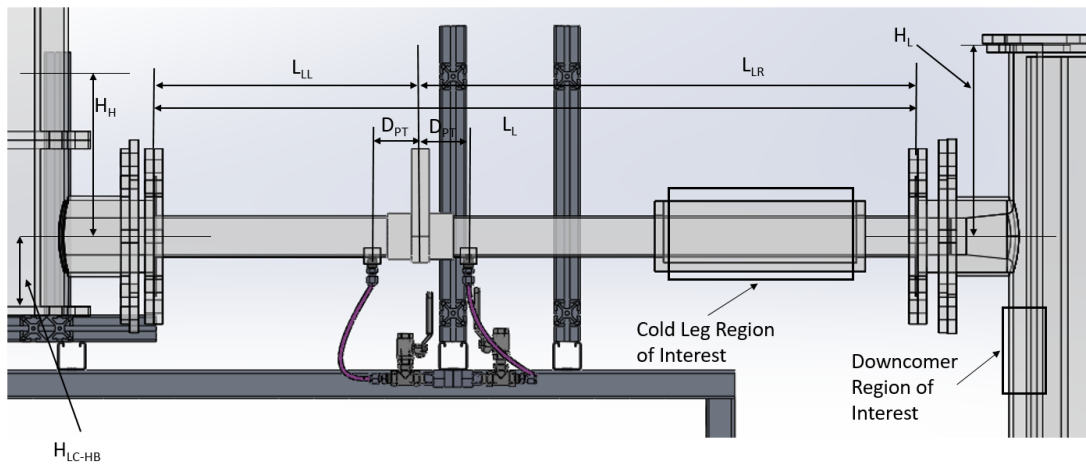


Figure 3.2: Vessel & Cold Leg Geometry.

	Symbol	Description	Dimension (cm)
Heavy Side Vessel	$ID_{HV}$	Inner Diameter of Heavy Vessel	34.29
	$H_{LC-HB}$	Leg Centerline to Bottom of Heavy Vessel	10.9
Cold Leg	$ID_{LC-HB}$	Inner Diameter of Cold Leg	5.31
	$L_L$	Total Length	130.81
	$L_{LL}$	Length of Left Section	39.37
	$L_{LR}$	Length of Right Section	91.44
	$D_{PT}$	Distance of Pressure Taps from Valve Midplane	15.98
Ligh Side Vessel	$ID_{LV}$	Inner Diameter of Outer Cylinder (Vessel)	34.29
	$OD_{LV}$	Outer Diameter of Inner Cylinder (Barrel)	30.48
	$H_{LC-LB}$	Cold Leg Centerline to Bottom Plate	80.33
	$H_{LC-LT}$	Cold Leg Centerline to Top Lid	27.94

Table 3.1: Dimensions of Vessels & Cold Leg.

It was proposed to implement a reactor-like geometry of the cold-leg and downcomer junction using some conical shape and a rounded edge. The top image of Figure 3.3 shows the nozzle sitting flush against the vessel wall, while the bottom image shows the nozzle dimensions to required to achieve a the best possible fit.

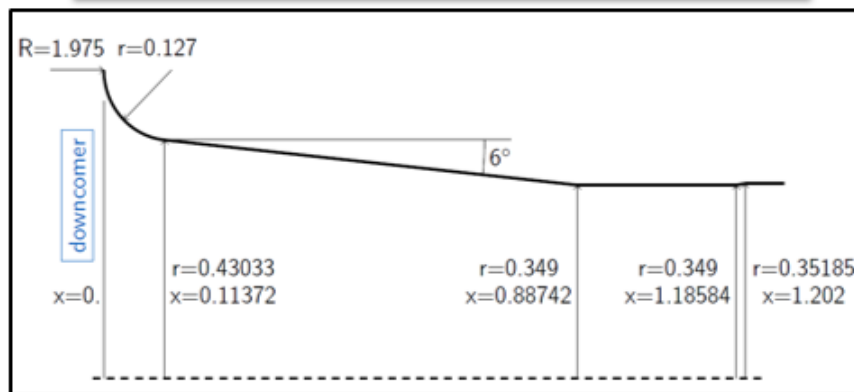
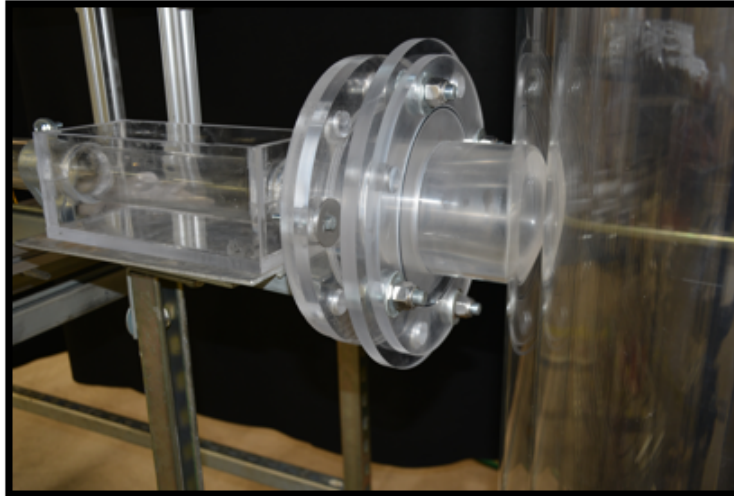


Figure 3.3: Cold Leg Vessel Nozzle.

A description of the facility drawings and fluid domain can be found in appendix A.

## 4. TEST CONDITIONS AND MEASUREMENT LOCATIONS

Two tests (identified as Open Test and Blind Test) were conducted under different test conditions. The OT was executed using two solutions with a target density difference of  $100 \text{ kg/m}^3$ . The BT was executed using two solutions with a target density difference of  $200 \text{ kg/m}^3$ .

### 4.1 Fluid Properties

To confirm that the refractive index remained constant during mixing of the selected solutions, the refractive index of a solution generated by the mixing of the two surrogates at different ratios was measured. In particular, density, viscosity, and index of refraction of the parent solutions and intermediate mixtures have been measured and reported in Table 4.1. One can observe that the index of refraction is stable while the two solutions mix. This condition is important when applying the flow visualization and measurements techniques. Densities were calculated by measuring the weight of a 10-ml sample taken from batch of solution maintained at a given temperature. The 10-ml volume is extracted using an electronic pipette. The weight of the sample taken is measured with an analytical balance accuracy. The sample is transferred to a glass beaker and placed on the plate of scale. Measurements were performed on solutions in thermal equilibrium with the laboratory environment temperature, at an average of  $21 \text{ }^\circ\text{C}$ . Viscosity was measured using a coupled with a double-couette cylindrical system to increase the surface area, yielding enhanced accuracy. The accuracy the instrumentation can be found in Table 4.1. Viscosity was measured at an ambient temperature of  $20.5 \text{ }^\circ\text{C}$ . Figure 4.1 shows the calculated densities of the surrogate fluids and the associated refractive index. Figure 4.2 presents the viscosity of the mixtures for both OT and BT. It can be seen that viscosity is a linear function of the mixture density. This function is displayed on the figure.

Fluid Properties of Sample Mixtures (Ethanol-Water : Salt-Water ) %*volumetric									
Sample	1	2	3	4	5	6	7	8	9
Ratio	100:0	87.5:12.5	75:25	62.5:37.5	50:50	37.5:62.5	25:75	12.5:87.5	0:100
Density (g/cm <sup>3</sup> )	0.95963	0.97057	0.9866	0.9975	1.00827	1.02575	1.03839	1.05235	1.0649
Viscosity (Pa·s)	0.002334	0.002182	0.002038	0.001875	0.001737	0.00155	0.001459	0.001282	0.001181
Refractive Index	1.3515	1.3505	1.3515	1.3513	1.3509	1.3510	1.3507	1.3510	1.3505

Table 4.1: Fluid Properties of Sampled Mixtures (OT).

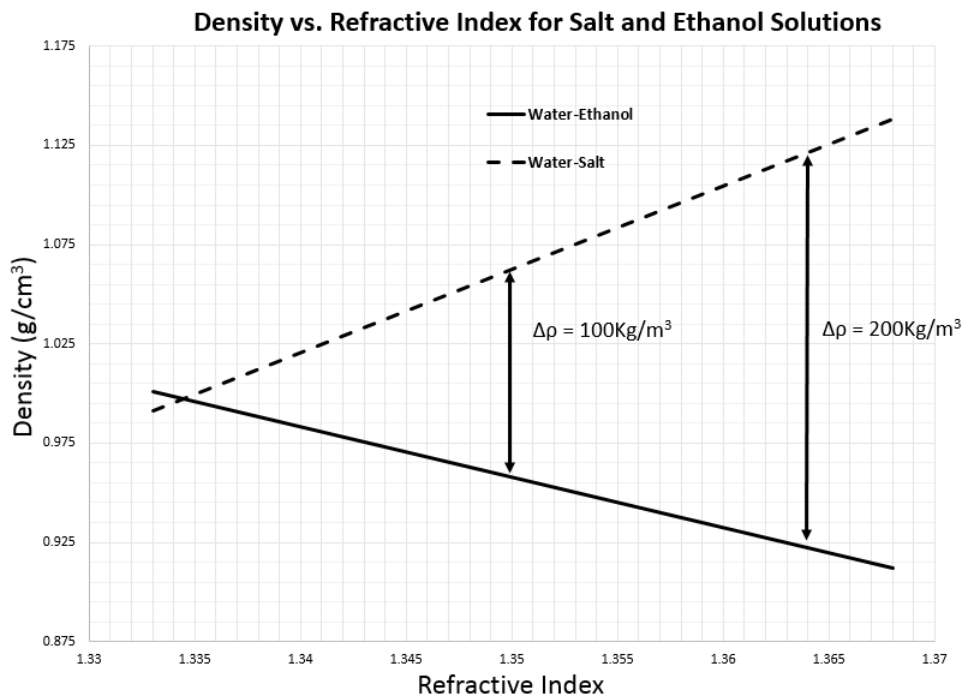


Figure 4.1: Density vs. Refractive Index of Solutions.



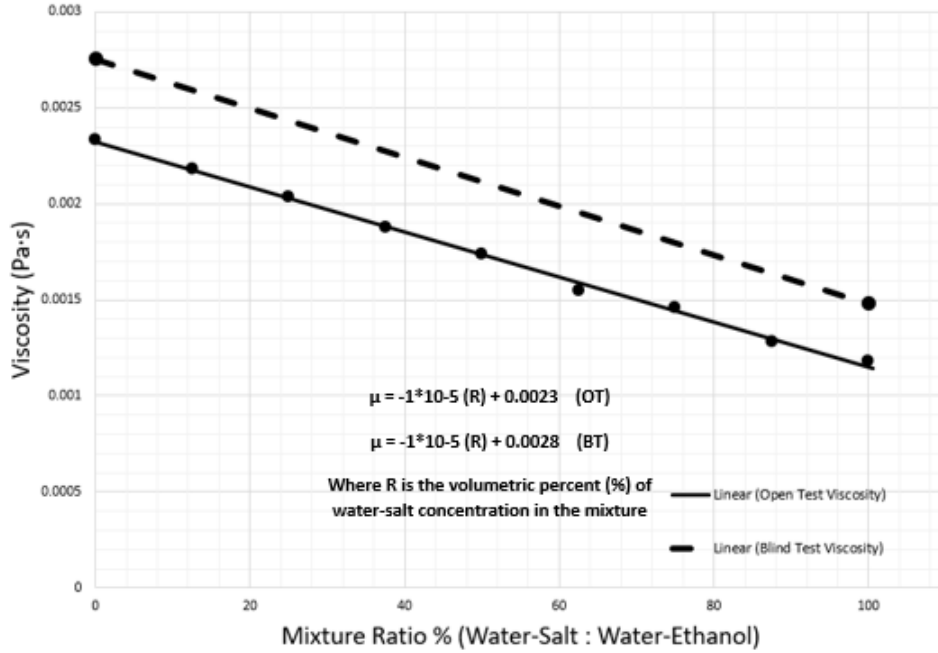


Figure 4.2: Viscosity of Fluids Mixtures.

All tests were performed with both solutions at a constant ambient temperature of  $21\text{ }^{\circ}\text{C} \pm 0.3$ . Figure 3.2 shows the liquid level labeled as Height of Heavy fluid ( $H_H$ ) and the Height of Light vessel labeled ( $H_L$ ). The OT and BT targeted test conditions can also be found in the appended documents. Boundary conditions for open and blind tests are summarized in Table 4.2. The height of the heavy fluid is calculated from the densities of the surrogate solutions, in order to equalize the pressure at the center-line across the isolation valve at the start of the test.

$$H_H = \frac{\rho_L}{\rho_H} H_L$$

where  $H_L$  is fixed to 27.9 cm.

	OT				BT			
	Density (kg/m <sup>3</sup> )	Viscosity (Pa·s)	Solution Concentration (Mass %)	H <sub>H</sub> (cm)	Density (kg/m <sup>3</sup> )	Viscosity (Pa·s)	Solution Concentration (Mass %)	H <sub>H</sub> (cm)
Heavy Fluid	1064.7	0.00109	9.5% salt mass	25.06	1110.7	0.001485	16.0% salt mass	22.99
Light Fluid	956.54	0.00245	26.0% ethanol mass		915.27	0.002755	46.0% ethanol mass	

Table 4.2: OT and BT Fluid Properties.

## 4.2 Measurement Locations

The location and dimensions of the two measurement/visualization windows, together with the reference coordinate systems are shown in Figure 4.3. The two windows are symmetric across their individual axes.

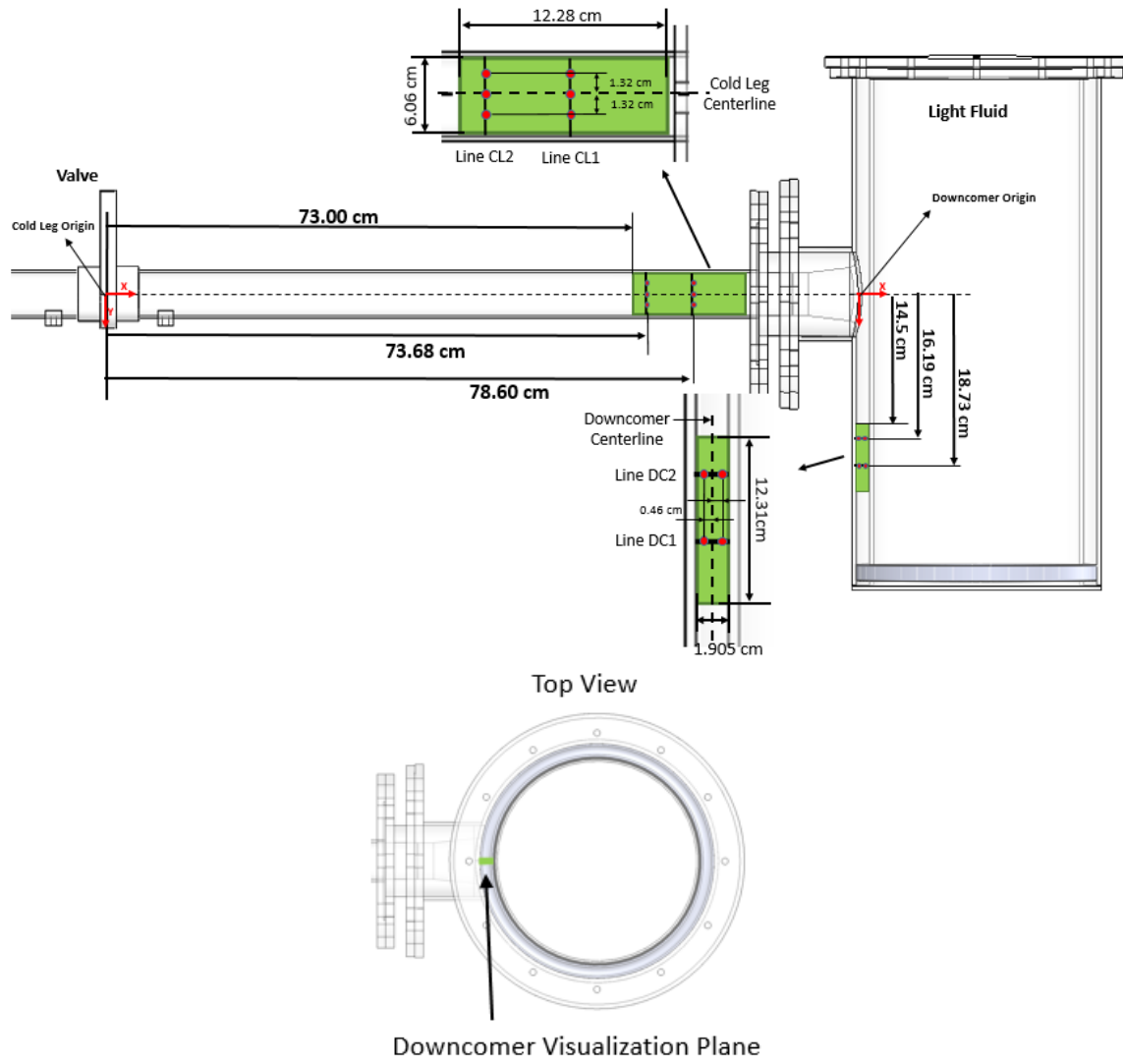


Figure 4.3: Visualization Windows.

In addition to the velocity and concentration, the pressure difference was measured across the isolation valve and recorded for the duration of the experiment. Figure 3.2 shows the location of the of the pressure taps.

## 5. EXPERIMENTAL METHODS AND MEASUREMENT TECHNIQUES

The experimental facility is designed to simulate the buoyancy driven flow between cold and hot water typical of cold water injection events taking place within the cold leg and the downcomer. The facility produces high fidelity experimental data in a prototypical geometry, to test uncertainty quantification methods in conditions closer to real reactor applications. To simulate the mixing phenomena of hot and cold water but also maintain low operating pressures and temperatures for practical reasons, two surrogate solutions of different densities were carefully chosen and prepared to represent the cold and hot fluids. The cold fluid is simulated using a solution of water and salt. A solution of water and ethanol was used to simulate the hot fluid. Concentrations of salt and ethanol in water were selected to achieve the desired density difference between the heavy and light solutions. Properties of the solutions (density, viscosity, and index of refraction) were measured and recorded before the test initiation.

Local variations of the refractive index (RI) in the flow cause potential issues when attempting to apply optical measurement techniques such as PIV and LIF. This issue can be resolved by RI matching. It was possible to find surrogate solutions of specific concentrations that at a given density difference that will result in matching refractive indexes. As discussed in the introduction, previous tests identified a combination of ethanol and sodium chloride (NaCl) to be the most suitable for experiments of a larger scale and it is therefore also chosen for this study. High resolution measurements of velocity and concentration fields were performed using specialized laser-based techniques.

### 5.1 Particle Image Velocimetry

PIV is a non-intrusive, laser based, optical measurement technique to quantify velocity vector fields of a fluid. The displacement of fluid elements is captured by using highly reflective, low density micro seeding particles that follow the fluid flow without impacting the flow characteristics. A laser sheet is used to illuminate the test section and particles. A series of images are captured

using a high resolution camera at a desired frequency. Images captured are processed using in-house codes, and a velocity vector field is constructed. These tracer particles scattered the laser light back to the PIV cameras as they passed through the laser sheets at the regions of interest.

Velocity vectors were retrieved by processing image pairs using PIV analysis software (Prana) [19] [20]. All PIV images captured by the 12-bit depth cameras were processed by the advance multi-pass, multi-grid PIV processing algorithms based on the robust phase correlation (RPC) algorithms implemented in the PRANA codes by Virginia Tech. A three step processing was applied. The initial interrogation window was a 64x64 pixel area, followed by two interrogation areas of 32x32 pixels. All passes had a 50% window overlap. Velocity vectors were calculated from the correlation map with a Gaussian peak fit for sub-pixel accuracy [21]. Each pass contained statistical validations erroneous vectors. A median filter [22] was applied, and standard deviations of the neighboring vectors were used to filter out spurious vectors, and blanks were filled by velocity interpolation.

The PIV measurement areas had 37x80 instantaneous velocity vectors in the cold leg region and 20x80 instantaneous velocity vectors in the downcomer region. The spacing of adjacent vectors at the cold Leg was 0.155cm. The spacing of the adjacent vectors at the downcomer was 0.105cm.

## **5.2 Laser Induced Fluorescence**

LIF is a laser based measurement technique used to measure temperature or concentrations of fluids. A soluble tracer dye is uniformly mixed with the fluid. A laser sheet illuminates the test section causing the particles to fluoresce. A series of images are captured using a high resolution camera. Concentration distributions can be constructed by converting the camera signal intensity into physical concentration from the images captured and processed using in-house codes. For this experiment, Rhodamine 6G (absorption peak at 532 nm and emission peak at 552 nm) was used as the tracer dye. This fluorescent dye was selected due to its negligible response to temperature changes that makes it suitable for concentration measurements.

### 5.2.1 LIF Calibration

The intensity of the light emitted by the dye was correlated to the concentration of the solutions by performing a 5-point in-situ calibration. Rhodamine 6G was dissolved to a parent heavy solution with the same concentration used during the test. From this parent solution (100% heavy solution calibration point), three additional solutions were prepared by mixing it with amount of light solutions. These solutions were used for the 75%, 50%, and 25% calibration points. One additional point was included to account for pure light solutions (0% calibration point). To apply the best possible calibration to the captured images, two calibration methods were attempted.

The first method involved using a single mean intensity value from a captured image for each calibration point. The average intensity is calculated by summing each pixel intensity and dividing by the total number of number of pixels.

$$I_{avg} = \frac{1}{N} \sum_{p=1}^N I_p \quad (5.1)$$

where  $I$  is the signal intensity,  $N$  is the total number of pixels, and  $p$  in the pixel index. By calculating the mean intensity for five known concentrations, a linear curve can be estimated to then apply to the open test and blind test. These plots can be seen in Figure 5.1 and Figure 5.2 for open test and blind test calibration.

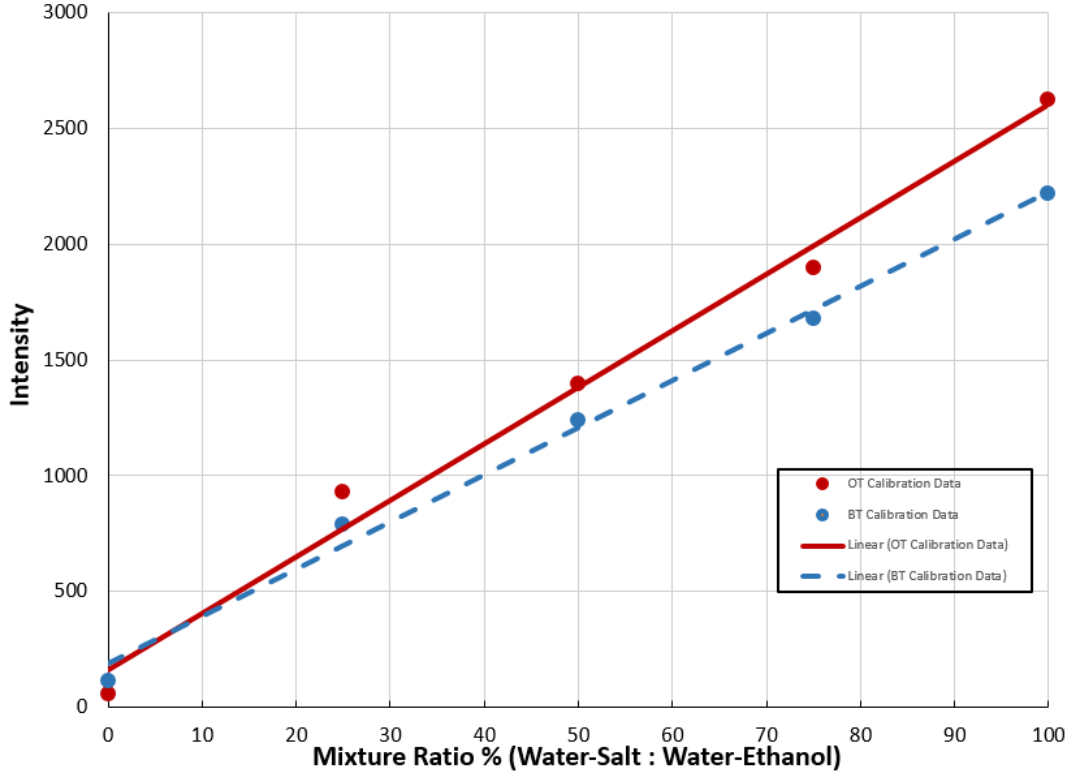


Figure 5.1: OT and BT LIF 5-Point Calibration Curve from Window Average Intensity.

On the plots, the slope represents the increasing intensity as the mixture ratio approaches 100% water-salt. The result is a linear expression for calculated the concentration.

$$C_{OT} = 0.0409 * I(i, j) - 6.484 \quad (5.2)$$

$$C_{BT} = 0.0489 * I(i, j) - 9.138 \quad (5.3)$$

The second method involved a local pixel intensity averaging from each calibration point. An 8 by 8 pixel area is averaged for the entire image size. This was applied to five known concentrations. A second degree polynomial fit was then applied to each coordinate for all concentrations from 0-100% mixture ratio.

$$C(X, Y) = A(X, Y) * I(i, j)^2 + B(X, Y) * I(i, j) + C(X, Y) \quad (5.4)$$

where C is the concentration at point, I is the intensity at a point, i,j are pixel indexes, and A,B,C are a two-dimensional coefficient matrices created by curve fitting. This process was repeated for open test and blind test. An example of the polynomial fit at the center point of an image with varying intensities is shown in Figure 5.3.

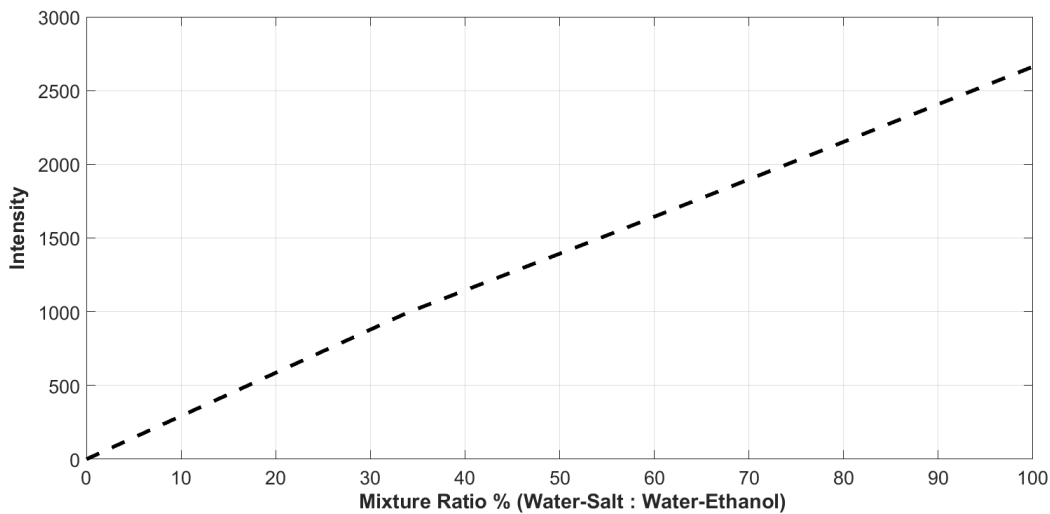


Figure 5.2: OT LIF 5-Point Local Calibration Curve for a single point in point in space.

Based on the calibration methods applied, the second polynomial curve was used to calculate fluid concentrations.

### 5.3 Experimental Method

PIV and LIF technique was used to capture the concurrent velocity and concentration fields in the cold leg region and PIV was used to capture the velocity vector field in the downcomer region, and a combined [23] [24] [25]. The solutions were uniformly seeded with silver-coated hollow glass spheres (mean diameter of 16  $\mu\text{m}$  and a density of 1.6  $\text{g cm}^{-3}$ ) to perform the PIV measurements. The PIV and LIF systems consisted of a laser source with appropriate optics to



create two 1-mm laser sheets at the regions of interest (Figure 4.2). Three digital CMOS cameras with a full resolution of 1280 x 800 pixel were used. Two cameras were installed to record PIV and LIF data at the cold leg, and one camera is used to record PIV data at the downcomer. Camera settings were optimized based on the visualization window and the flow observations performed during shakedown tests (1280 x 600 resolution at the leg and 1280 x 320 at the downcomer). Fluorescent dye (Rhodamine 6G) was homogeneously mixed with the heavy solution to perform concentration measurements using LIF. This preparation was completed earlier enough from the test initiation to allow the solutions to reach thermal equilibrium with the laboratory environment. Two thermocouple probes were utilized to monitor and measure the temperature of the heavy and light solutions respectively, before and during the experiments. Pressure across the isolation valve was verified at the beginning of each test and monitored and recorded during the duration of the tests using a high accuracy differential pressure transducer.

With the isolation valve closed, the light solution was transferred into the light vessel to be completely filled up to the level of the top lid. The heavy solution was then transferred into the heavy vessel up to a level estimated to balance the hydrostatic pressure across the center line of the isolation valve. Air pockets formed during the fluid transfer were carefully removed before each test. The experiment was initiated by releasing the spring mechanism connected to the isolation valve which lifted the guillotine valve, and trigger the visualization systems. Camera recording start times and durations were optimized based on the observed arrival and transition times of the heavy fluid front during previous shakedown tests. The LIF camera was set next to the PIV camera at a small angle as seen in Figure 5.3. The frame of the LIF images contained that of the PIV images.

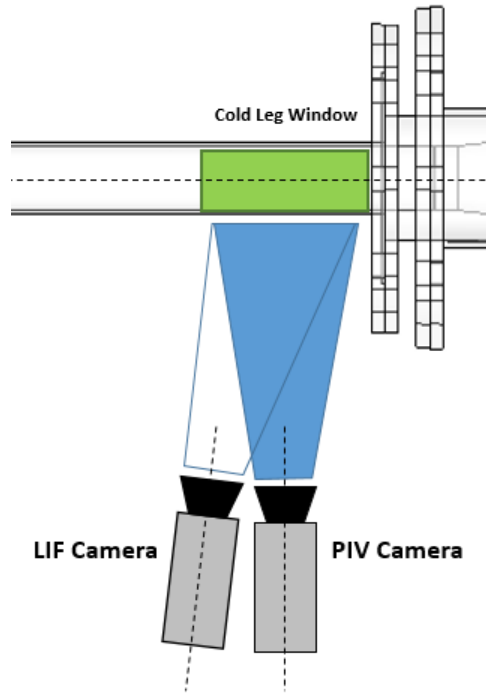
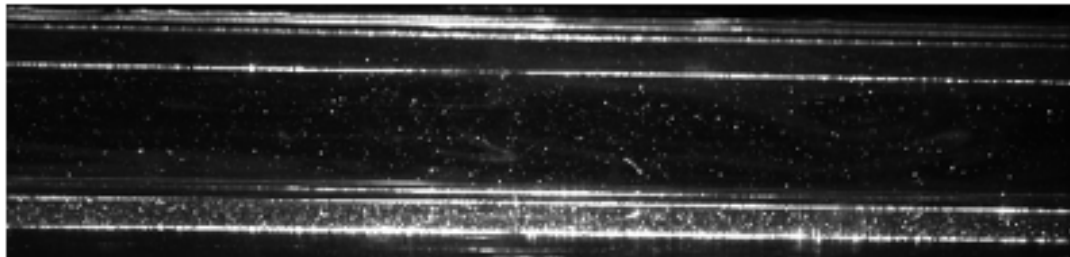


Figure 5.3: Camera Setup for Cold Leg Window.

To avoid interference between the two techniques, the LIF camera was fitted with a 590nm bandpass filter that allowed for the Rhodamine-6G emission wavelength to pass and reflected the laser light scattered from the particles. Similarly the PIV camera was fitted with a 532nm bandpass filter that allowed laser light scattered from the particles to pass but reflected fluorescent light. Figure 5.4 shows two images with and without the appropriate light filters. Figure 5.5 shows the camera system being applied to the colg leg and downcomer for PIV only.



a)



b)

Figure 5.4: a) Image without 552nm Light Filter. b) Image with 552nm Light Filter.

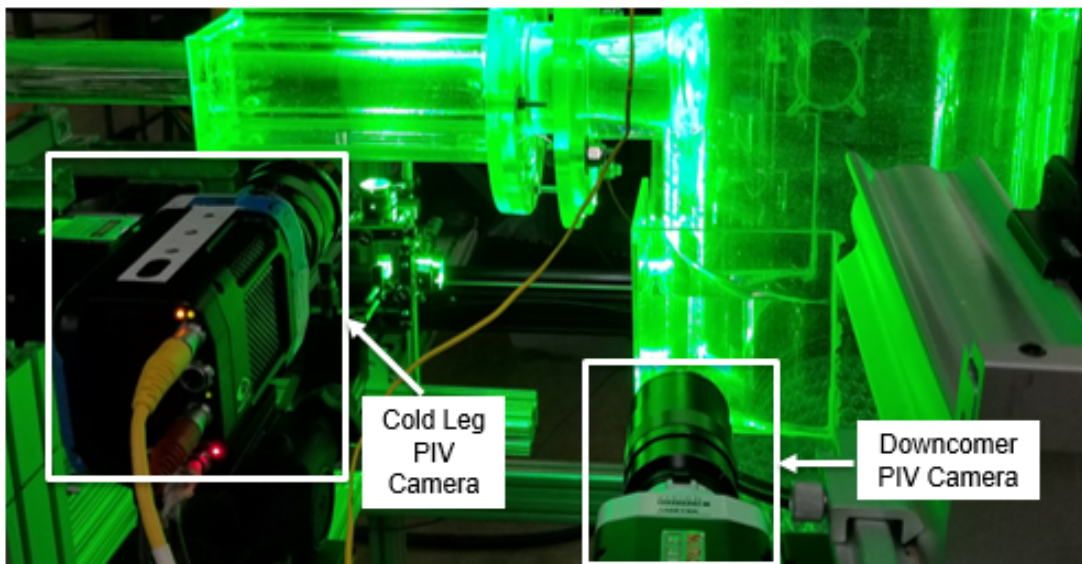


Figure 5.5: Camera System for Simultaneous PIV Measurements.

A full list of the equipment and instrumentation used during experiments can be found in Table

5.1.

#	TYPE	MODEL	PURPOSE	ACCURACY	COMMENTS
1	CAMERA	Phantom MIRO M310	Capture Images for LIF in Cold Leg Region	N/A	OT: 250 frames/sec BT: 500 frames/sec
2	CAMERA	Phantom MIRO M310	Capture Images for PIV in Cold Leg Region	N/A	OT: 250 frames/sec BT: 500 frames/sec
3	CAMERA	Phantom MIRO M310	Capture Images for PIV in Downcomer Region	N/A	OT: 250 frames/sec BT: 500 frames/sec
4	Pressure Transducer	OMEGA:MMDWB10W BIV5P2D0T2A2CE	Measure Pressure Drop across Isolation Valve	$\pm 0.361$ PSID (Pressure Range)	
5	Thermocouple	K Type	Measure temperature at bottom of heavy water tank	Standard: $\pm 2.2$ C or $\pm .75\%$	Temperature was measured to be $20.5$ °C $\pm 0.3$ °C
6	Thermocouple	K Type	Measure temperature at top of light water annulus	Standard: $\pm 2.2$ C or $\pm .75\%$	Temperature was measured to be $20.5$ °C $\pm 0.3$ °C
7	DAQ	NI SCXI-1303	Collect pressure/temperature Data		1000Hz sampling rate
8	Laser	CHANGCHUN NEW INDUSTRIES MGL-W-532 20W	Create LIF/PIV Laser Sheet		Continuous Laser
9	Mass Scale	Mettler Toledo AB analytical balance (Model. AB204-S)	Measure mass of samples	$\pm 0.0001$ g	
10	Pipette	Eppendorf Repeater Xstream	Measure fluid volume	$\pm 0.055$ ml	
11	Rheometer	MCR 300 Modular Compact Rheometer	Measure viscosity of working fluids	$\pm 0.5\%$	Viscosity is measured at $22.4$ °C
12	Refractometer		Measure Refractive Index	$\pm 0.0005$	RI is measured at $22.4$ °C
13	LaVision Filter	LIF camera Filter for CL region	Filter light coming from PIV particles	BP590nm-67FWHM	
14	Edmund Filter	PIV camera Filter for CL region	Filter light coming from LIF dye	BP532nm-10FWHM	

Table 5.1: Equipment and Instrumentation Specification.

## 6. RESULTS AND ANALYSIS

Each test produced pressure drop data across the isolation valve as well as instantaneous velocity and concentrations within the measurement windows. The experimental results are presented in terms of pressure drop, heavy front velocity, time-averaged velocity magnitude, time-averaged velocity profiles on selected lines and time averaged concentrations. One probe line marked inside each window (Figure 4.3 CL1, DC1,) was selected to plot velocity and concentration profiles.

A total of eleven test were conducted, two were visualization/shakedown test, five of which were open test, and four blind test. The following (Table 6.1) provides the list of test.

Test	PIV		LIF	Pressure
	Cold Leg	Downcomer	Cold Leg Only	
<b>OT3</b>	Available	Available	Not Available	Available
<b>OT5</b>	Available	Not Available	Available	Available
<b>BT3</b>	Available	Available	Available	Available
<b>BT4</b>	Available	Available	Available	Available

Table 6.1: List of Test and Available Data.

### 6.1 Pressure Drop

The pressure measurements collected during the tests showed similar trends under both test conditions (Figure 6.1). During the time of the valve opening, there are pressure oscillations generated by the valve opening mechanism. Higher pressure difference across the isolation valve was observed during the BT, due to the higher density difference between the working fluids. In both

tests, the pressure difference approaches to zero as the fluids mix inside the cold leg pipe and the density difference is reduced.

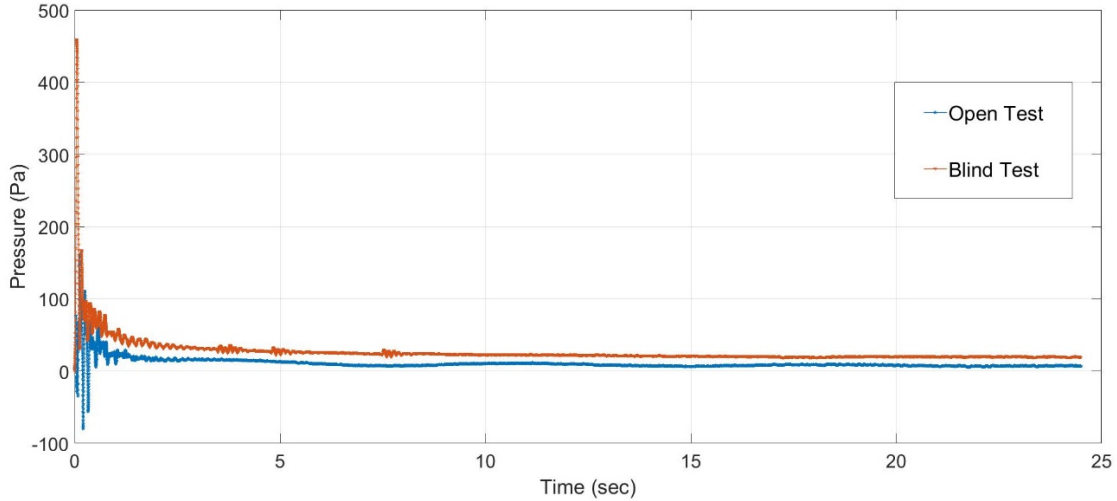


Figure 6.1: Pressure Difference across Valve.

## 6.2 Heavy Front Velocity

Density driven currents and lock-exchange flow exercises have been thoroughly investigated and modeled [26] [27]. The derivation of the front velocity can be analytically solve using the two assumptions, viscous dissipation is neglected, and the kinetic energy associated with the front is balanced by the loss is potential energy [28]. The following expression gives the theoretical value for the heavy fluid front velocity:

$$U_H = \frac{1}{2} \sqrt{g'D} \quad (6.1)$$

where,

$$g' = \left( \frac{\rho_H - \rho_L}{\rho_{avg}} \right) g \quad (6.2)$$

and D is the hydraulic diameter. Using this expression, the calculated heavy fluid velocities for the open and blind test were 11.79 cm/s and 15.85 cm/s, respectively.

The heavy fluid front was tracked as it moved across the visualization window in the cold leg region. The front position as a function of the time for OT and BT is plotted in Figure 6.2. The position is recorded from the time the heavy front enters the visualization window ( $t = 0$ s). The slope of the plot represents the average heavy fluid velocity of the front. The average velocities were found to be 9.99 cm/s and 14.34 cm/s for OT and BT respectively.

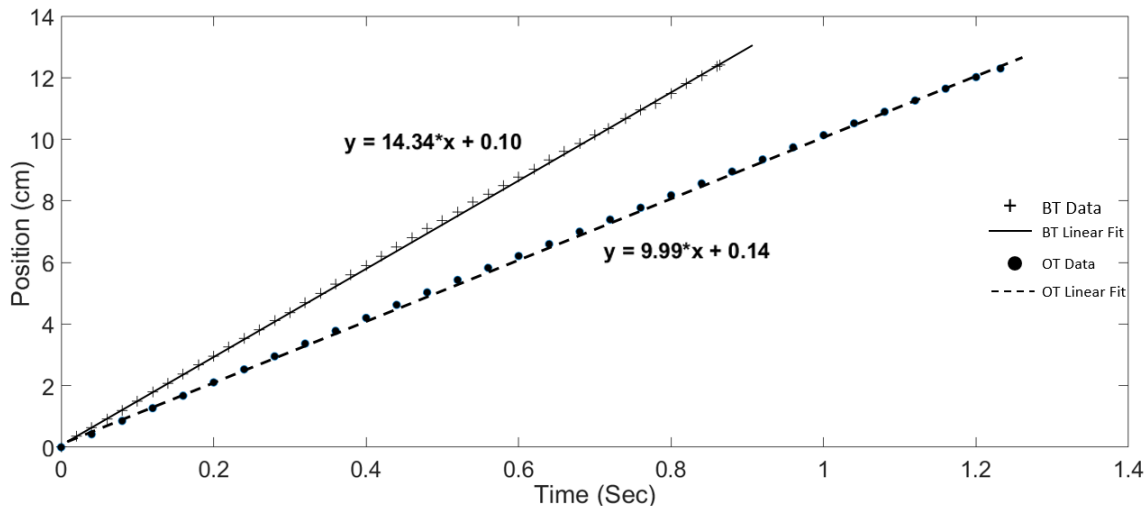


Figure 6.2: Cold(Heavy) Fluid Front Velocity.

The values found for the open and blind test agree with those calculated. The open and blind test have a percent difference of 15.3% and 10.5%, respectively. As expected, it was observed that the calculated theoretical value was larger than the measured values. This is due to the fact that viscous dissipation is neglected and kinetic energy losses to mechanical systems were ignored in the derivation.

### 6.3 Open Test Velocity and Concentrations Results

Data from OT5 is shown below for PIV and LIF results in the cold leg. However, due to reflections presenting difficulties in the downcomer, OT3 results are shown for PIV in the downcomer. PIV Results shared for OT3 can be found in the appended document "TAMU-PTSUQ-OT3-Rev1.1"

### 6.3.1 Cold Leg PIV and LIF Results

The time-averaged velocity magnitude contour at the cold leg is shown in Figure 6.3. The velocities represented in the figure are time-averaged from the time the heavy front enters the visualization window ( $t = 6.76$  s) until the end of the recording ( $t = 44.48$ s).

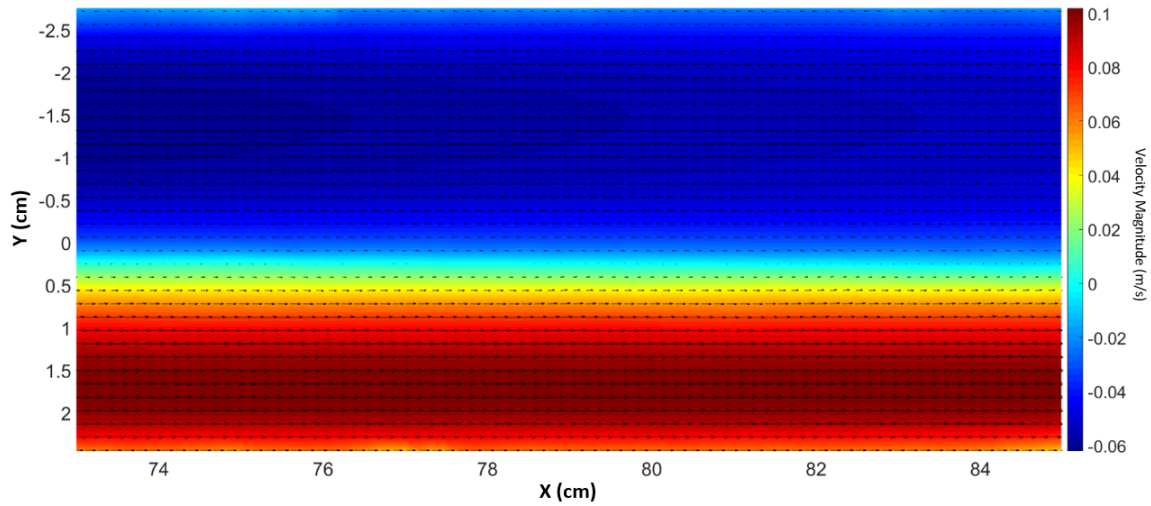


Figure 6.3: OT Cold Leg Time-Averaged Velocity Magnitude Contour.

The time-averaged horizontal velocity profiles along the line CL1 is plotted on Figure 6.4.



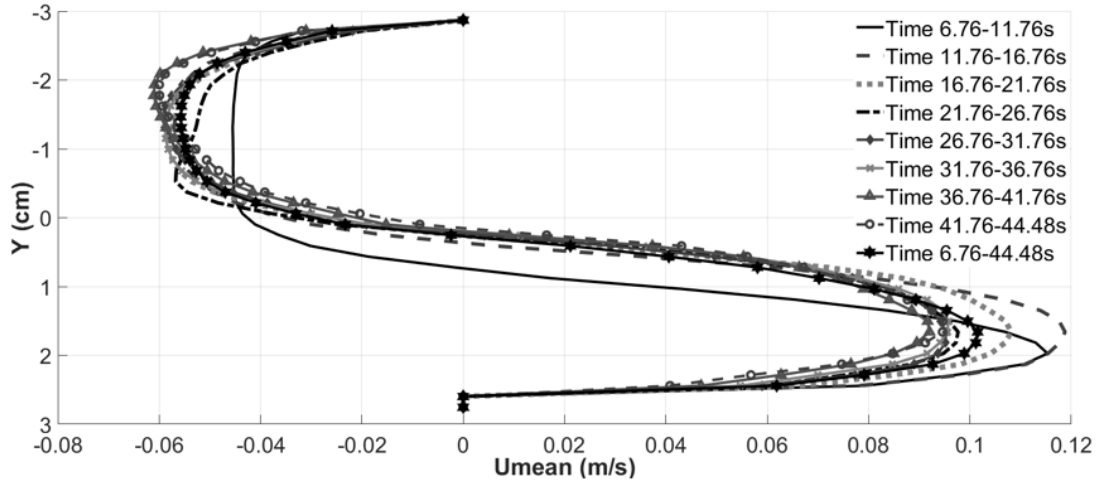


Figure 6.4: OT Cold Leg Velocity Profiles Computed at CL1 for Various Temporal Durations.

The instantaneous volumetric concentration field of the heavy fluid is shown in Figure 6.5 together with the concurrent instantaneous velocity vector field at different times. When the heavy front enters the visualization window, near the middle, exiting and near the end of the recording. Kelvin-Helmholtz instabilities can be seen developing on the interface between the two opposing streams. Figure 6.5 shows how the fluid interface assumes a wave profile near the end of the recording. No instabilities can be seen on the interface at this point.

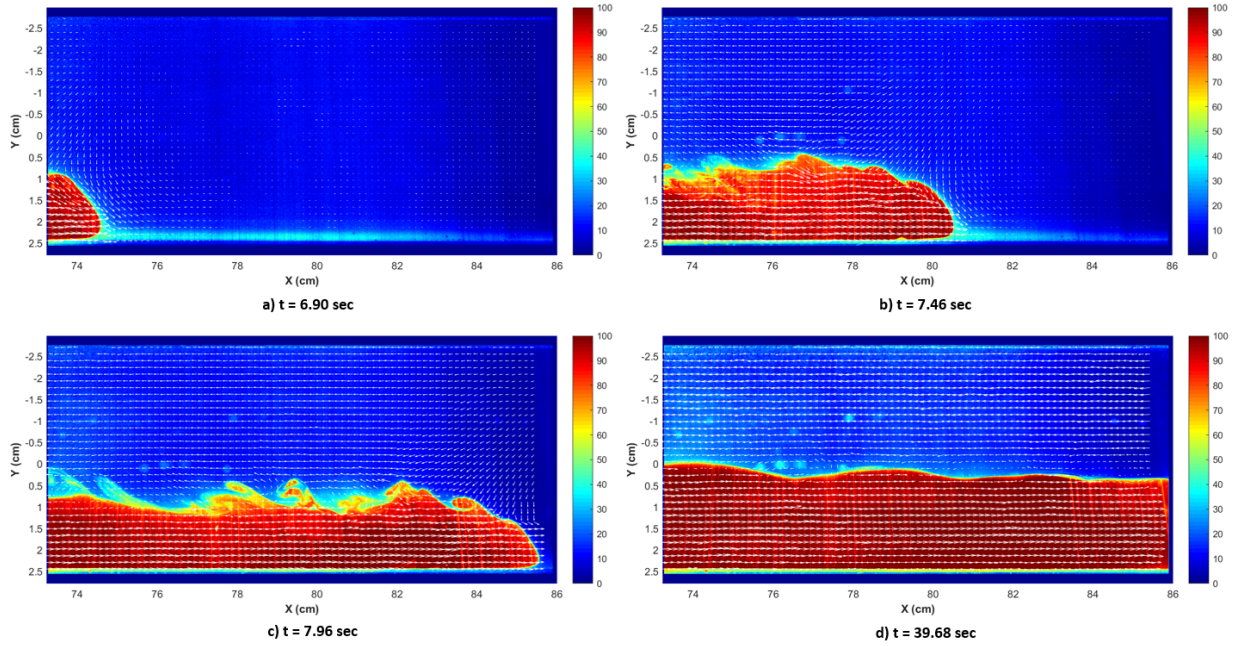


Figure 6.5: OT Cold Leg LIF and PIV Results.

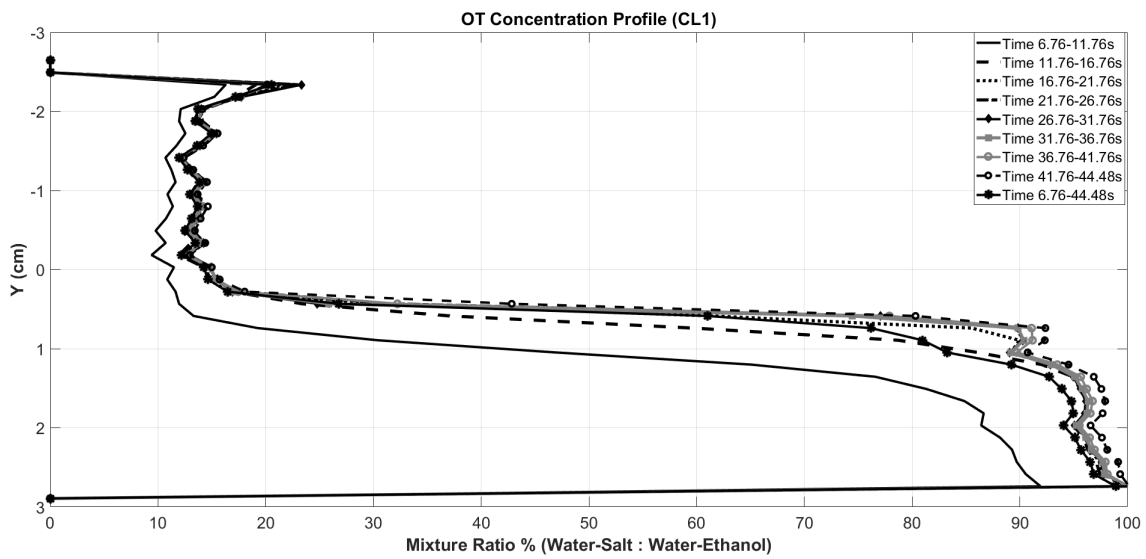


Figure 6.6: OT Cold Leg Concentration Profiles at CL1.

### 6.3.2 Downcomer PIV Results

The downcomer time-averaged velocity magnitude contour is shown in Figure 6.8. The velocities represented in the figure are time-averaged from the time the heavy front enters the PIV visualization window ( $t = 10.84\text{s}$ ) until the end of the recording ( $t = 50.48\text{s}$ ).

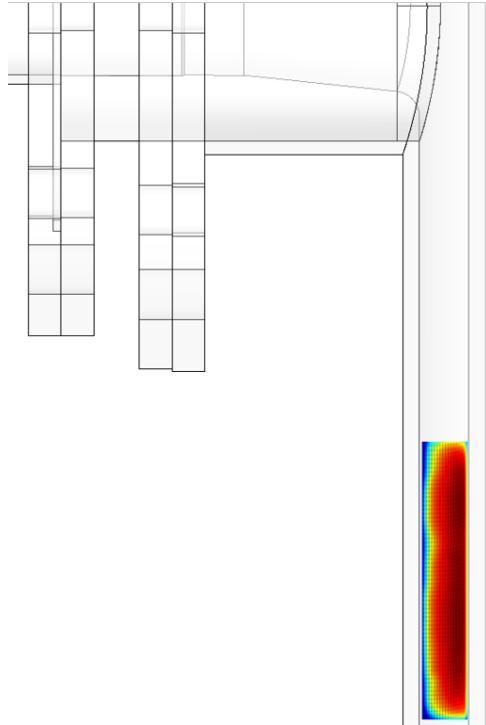


Figure 6.7: OT Downcomer Velocity Magnitude Contour.

The PIV results are presented horizontally (Figure 6.8), but actual fluid flow is vertical within the vessel as shown in Figure 6.7. This applies for the open and blind test results presented.

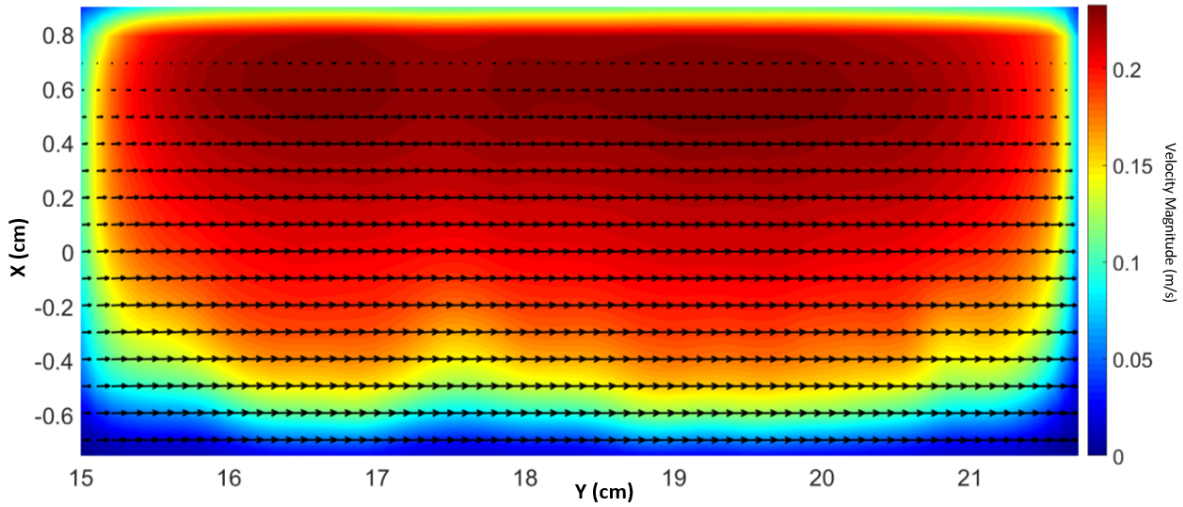


Figure 6.8: OT Downcomer Velocity Magnitude Contour.

The time-averaged vertical velocity profiles at DC1 are plotted in Figure 6.9.

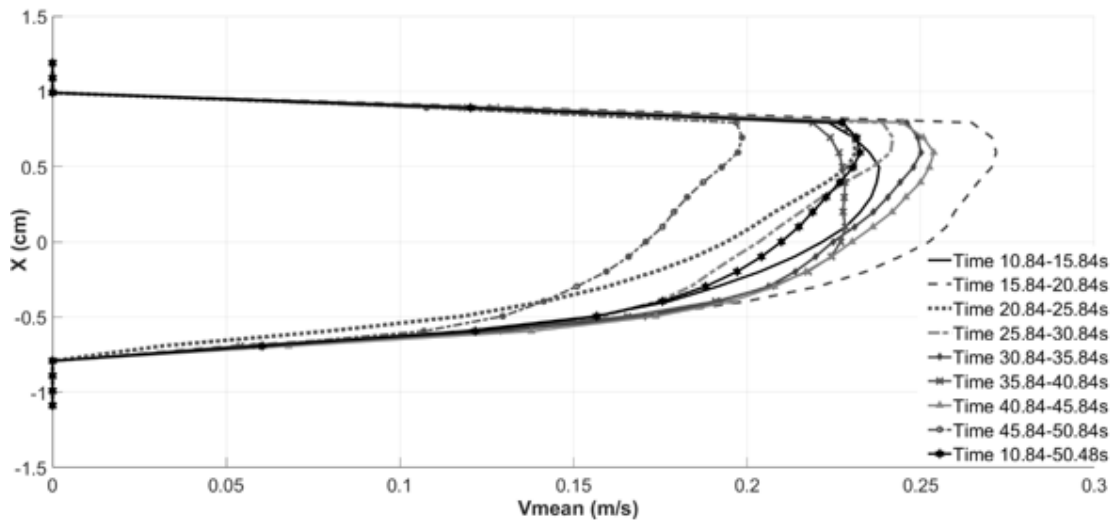


Figure 6.9: OT Downcomer Vertical Velocity Profiles Computed at DC1 for Various Temporal Durations.

## 6.4 Blind Test Velocity and Concentrations Results

### 6.4.1 Cold Leg PIV and LIF Results

The cold leg time-averaged velocity magnitude contour is shown in Figure 6.10. The velocities represented in the figure are time-averaged from the time the cold front enters the visualization window ( $t = 4.79$  s) until the end of the recording ( $t = 22.24$ s).

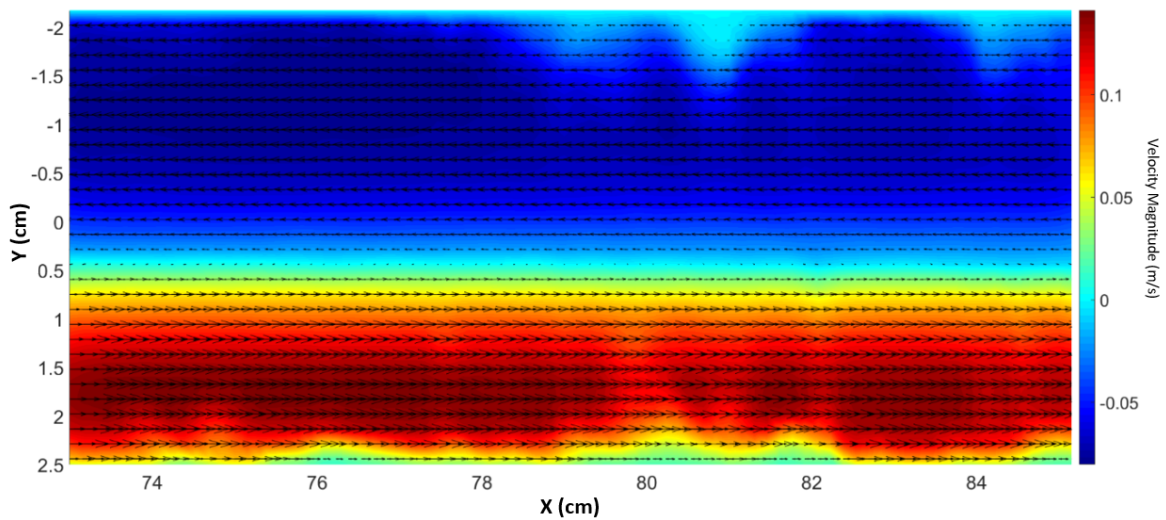


Figure 6.10: BT Cold Leg Time-Averaged Velocity Magnitude Contour.

The time-averaged horizontal velocity profiles at CL1 are plotted in Figure 6.11.

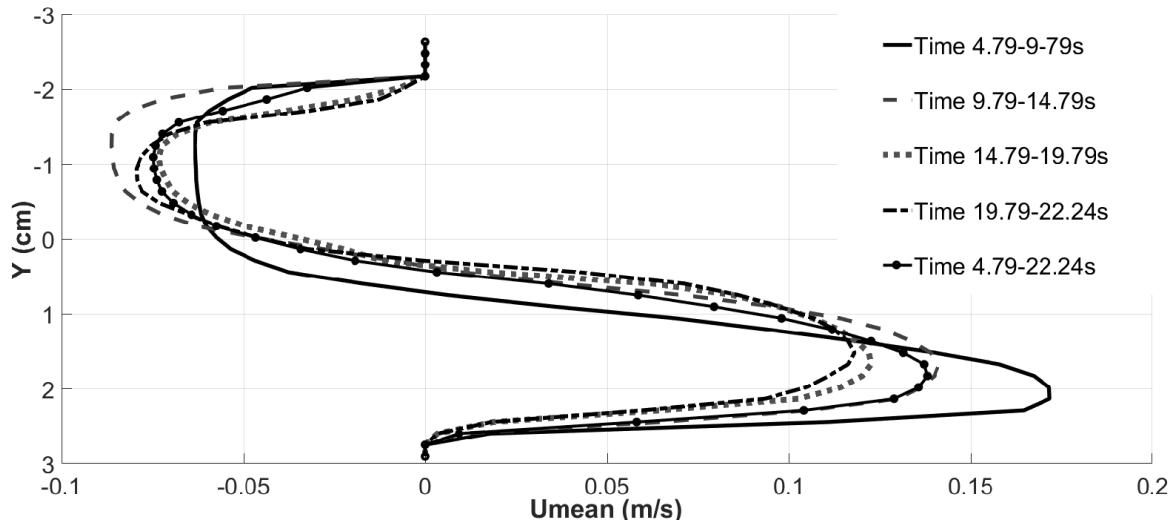


Figure 6.11: BT Cold Leg Velocity Profiles Computed at CL1 for Various Temporal Durations.

The instantaneous volumetric concentration field of the heavy fluid is shown in Figure 6.12 together with the concurrent instantaneous velocity vector field at different times. When the heavy front enters the visualization window, near the middle, exiting and near the end of the recording.

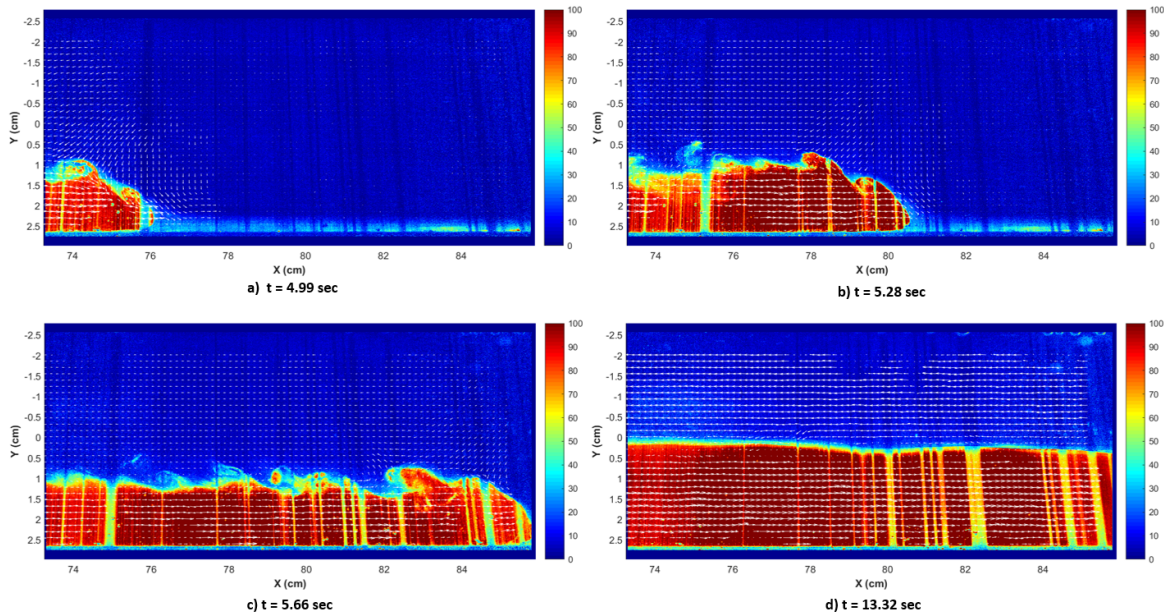


Figure 6.12: BT Cold Leg LIF and PIV Results.

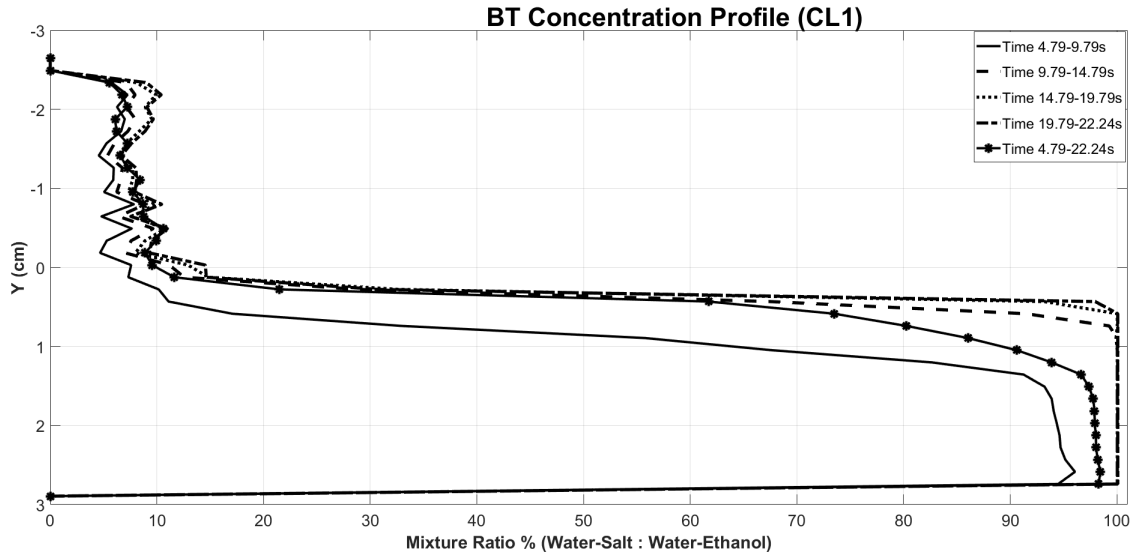


Figure 6.13: BT Cold Leg Concentration Profiles at CL1.

#### 6.4.2 Downcomer PIV Results

The downcomer time-averaged velocity magnitude contour is shown in Figure 6.15. The velocities represented in the figure are time-averaged from the time the cold front enters the PIV visualization window ( $t = 9.98\text{s}$ ) until the end of the recording ( $t = 41.01\text{s}$ ).

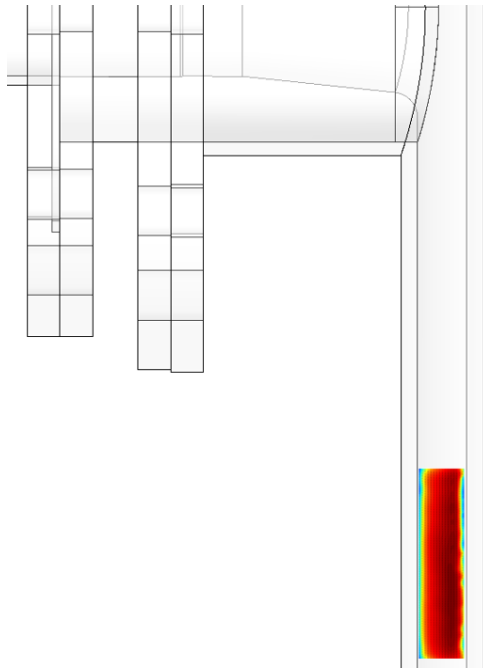


Figure 6.14: OT Downcomer Velocity Magnitude Contour.

As mention in section 6.3.2, PIV results are presented horizontally (Figure 6.15), but actual fluid flow is vertical within the vessel as shown in Figure 6.14.

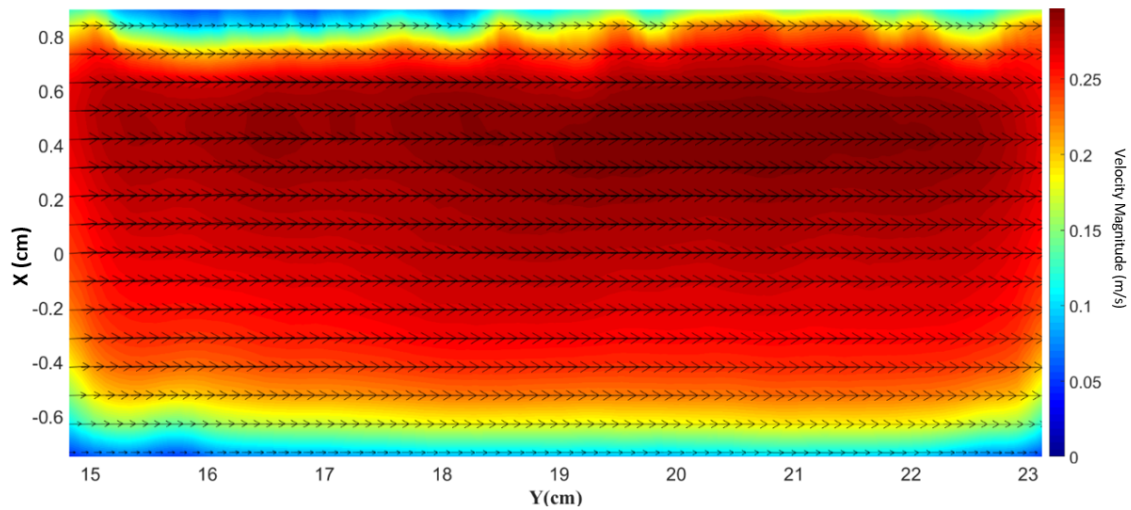


Figure 6.15: BT Downcomer Velocity Magnitude Contour.



The time-averaged vertical velocity profiles at DC1 are plotted in Figure 6.16.

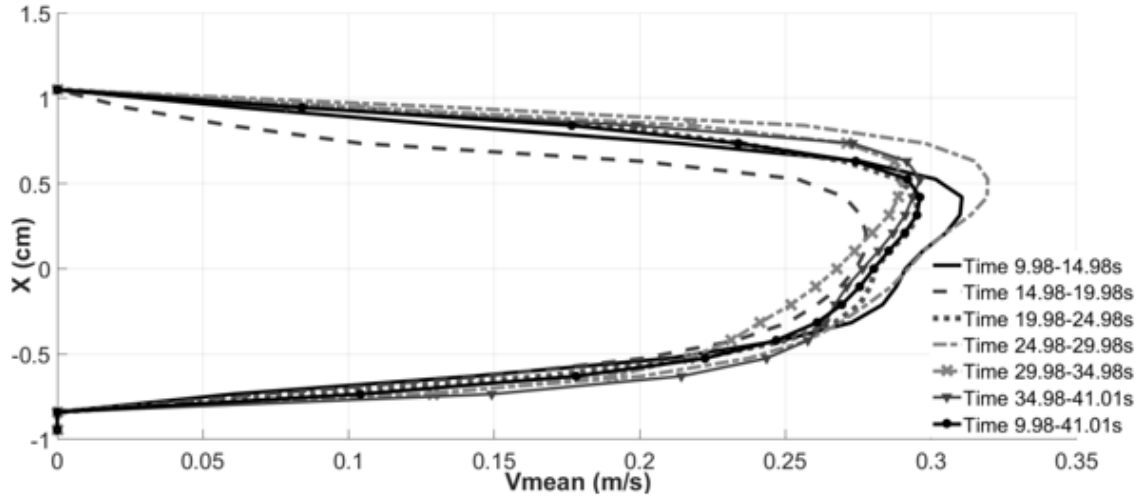


Figure 6.16: BT Downcomer Vertical Velocity Profiles Computed at DC1 for Various Temporal Durations.

## 7. UNCERTAINTY ANALYSIS

### 7.0.1 PIV Uncertainty

PIV uncertainty analysis employs the method applied in [29]. Calculated velocity can be expressed as,

$$U = \alpha \left( \frac{\Delta X}{\Delta t} \right) + \delta U \quad (7.1)$$

where  $\Delta X$  is the displacement of particle images,  $\Delta t$  is the time interval of successive images,  $\alpha$  is the magnification factor identified through a calibration, and  $\delta U$  are the uncertainty factors of flow field. The uncertainty of the measured velocity can be calculated by propagating the uncertainties of alpha, position, time, and  $\delta U$ .

$$\sigma_U = \sqrt{\left( \frac{\Delta x}{\Delta t} \right)^2 \sigma_\alpha^2 + \left( \frac{\alpha}{\Delta t} \right)^2 \sigma_{\Delta x}^2 + \left( \frac{\alpha \Delta x}{\Delta t^2} \right)^2 \sigma_{\Delta t}^2 + \sigma_{\delta U}^2} \quad (7.2)$$

where,

- $\alpha$ : Magnification factor estimated by in-situ calibration.
- $\sigma_{\Delta x}$ : Displacement uncertainty determined by the performance of PRANA code.
- $\Delta t_{OT}$ : Time interval uncertainty determined by camera settings.
- $\sigma_{\delta U}$ : Uncertainty factors of flow field estimated by particle density and diameter.

The magnification factor  $\alpha$  is estimated by in-situ calibration. The conversion from pixels to milometers was performed by taking calibration images of targets with known physical dimensions. Images captured during calibration gave correlated pixels to a physical distance of  $\alpha_{CL} = 0.0962$  mm/pix for the cold leg OT and BT. Downcomer calibration images gave  $\alpha_{DC} = 0.0655$  mm/pix for OT and BT. Image and lens distortions create slightly varying magnification factors.

This results in  $\sigma_{\alpha,CL} = 0.000617$  mm/px and  $\sigma_{\alpha,DC} = 0.000276$  mm/px for the for OT and BT, respectively.

The uncertainty from the vectors calculated is determined by the performance of PRANA code which has been thoroughly studied [30] [31]. These studies have reported an overall uncertainty of  $\sigma_{\Delta x}$  approximately 0.1 pixels. The spurious and erroneous vectors were evaluated for all Time-Resolved PIV velocity vectors. For all test, OT and BT, less than 1.5% of vectors were erroneous.

	<b>Cold-Leg</b>	<b>Downcomer</b>
<b><math>\alpha</math> (mm/pix)</b>	0.0962	0.0655
<b><math>\sigma_{\alpha}</math> (mm/pix)</b>	0.000617	0.000276
<b><math>\sigma_{\Delta x}</math> (pix)</b>	0.1	0.1

Table 7.1: Values Used for OT and BT Uncertainty Analysis.

The time interval between frames recorded by the high speed camera used during the experiment is  $\Delta t$ . The cameras recorded images at a rate of:  $f_{OT} = 250$  Hz and  $f_{BT} = 500$  Hz. Subsequently,  $\Delta t_{OT} = 0.004$  s and  $\Delta t_{BT} = 0.002$  s. The uncertainty given by the camera settings is 1% which corresponds to  $\sigma_{t,OT} = 0.04$  ms and  $\sigma_{t,BT} = 0.02$  ms.

The value  $\sigma_{\delta U}$  can be considered negligible as it describes the behavior of the particles in the fluid. As mentioned is chapter 5, the particle's diameter and density are sufficiently small and light to properly follow the fluid flow.

Overall, uncertainty analysis for the the OT and BT were performed assuming the maximum amount of error. Note that the same approach is taken for the vertical V components, and uncertainties can be calculated. The maximum error for PIV measurements for OT and BT were calculated to be,

$$\sigma_{CL,max} = 0.0027m/s$$

$$\sigma_{DC,max} = 0.0031m/s$$

Standard deviation of the velocity is described in the appended documents.

## 7.0.2 LIF Error Sources

LIF uncertainties are less commonly studied as it is difficult to quantify. In this case, an in situ calibration was performed using five points as previously discussed in chapter 5. After thorough investigation, it was observed that one of the main contributors to error in the LIF data was due to the volume of dye homogeneously mixed during calibration. Systematic errors that contributor to LIF measurements include background light, laser power fluctuations, spatial variation of light intensity, and camera sensor saturation. In order to measure qualitatively the background and laser light, 10000 images were taken of the facility without any fluorescent dye. Figure 7.1 shows recorded background intensities were small. This error can be eliminated by subtracting background images.

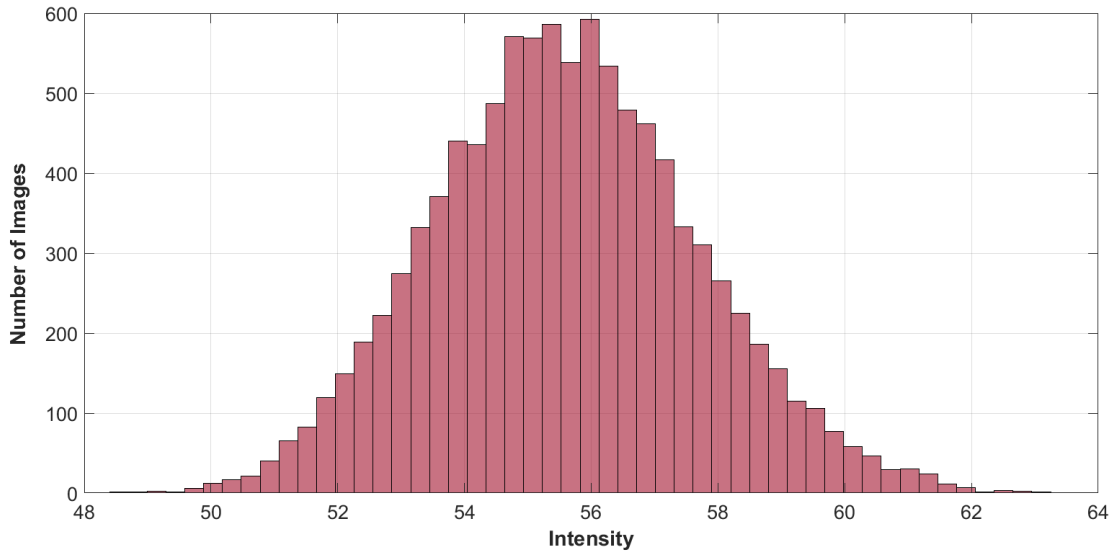


Figure 7.1: Background Intensity Distribution.

The laser power distribution also contributes to measurement error as damaged optical lenses and/or a fluctuating laser will create irregularities in the laser sheet. In addition, small scratches on wall surfaces, micro-bubble formation, and debris will obstruct the laser sheet and cast shadows within the test section. Figure 7.2 and Figure 7.3 demonstrate the effects of laser power fluctuations and spatial distributions on captured images.

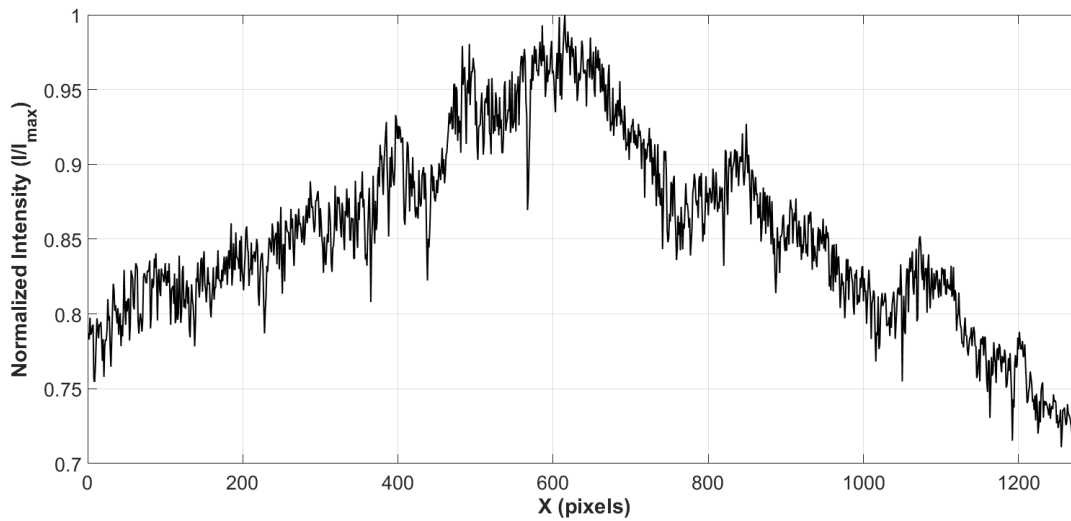


Figure 7.2: Normalized Intensity Along Horizontal Profile.

As seen in figure 7.2, the laser light intensity reaches a maximum near the center of the frame, and tails off as it moves towards the either edge of the frame.

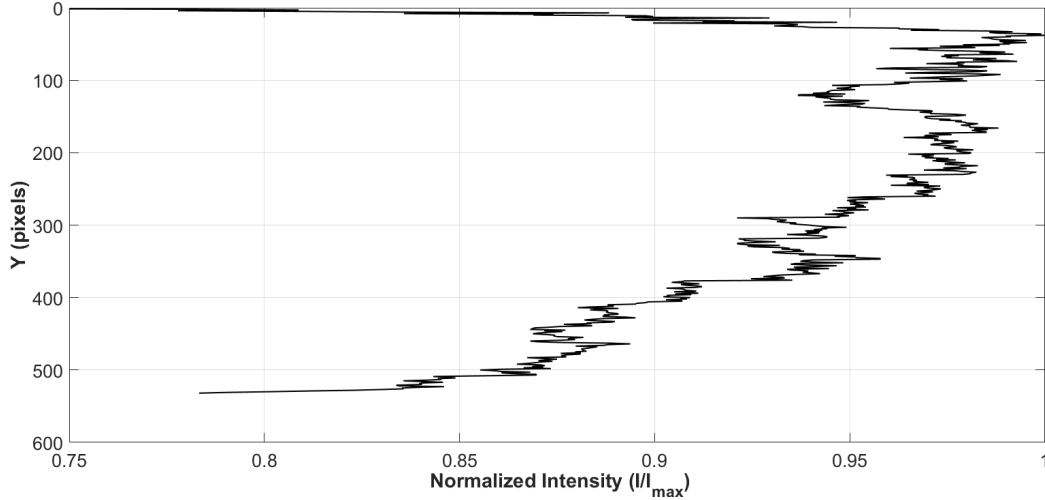


Figure 7.3: Normalized Intensity Along vertical Profile.

The laser spatial distribution is also affected in the vertical direction shown in Figure 7.3. Laser light entering from the top of the visualization window will be attenuated and decrease in intensity as it traverses through the plane. The camera sensor saturation was tested by increasing the concentration of Rhodamine-6G in small increments. To avoid saturating the camera sensor, the amount of Rhodamine-6G injected was selected approximately 65% of the maximum allowable before complete saturation.

The error sources posed a challenge when attempting to quantify into a factor. Therefore, all experiments were performed in situ. In addition, local calibration aids in minimizing these effects. By knowing the target concentration during the calibration and the calculated concentration based on the local point-by-point method, the relative error can be calculated by the following expression [32].

$$\epsilon = \frac{|C_o - C_p|}{C_o} * 100 \quad (7.3)$$

where  $C_o$  is the known concentration, and  $C_p$  is the calculated concentration using the local method. Applying this to a sample set of 5000 images of a known 50% water-salt calibration produced an average relative error of  $\epsilon_{OT} = 3.64 \%$  and  $\epsilon_{BT} = 4.62 \%$ . Standard deviation of the

concentrations were calculated similarly to the velocity.

## 8. CONCLUSION

The resulting fluid volumes at the end of the mixing assume the distribution shown in Figure 7.1. Food coloring observations and data taken from OT and BT allows for the following statements and assumptions.

The volumetric flow rate of the two opposing streams is obviously identical as long as the level inside the heavy fluid tank and light fluid annulus remains constant, assuming the system remained airtight during the duration of the experiment. As the fluids mix, the mixing rate drops, the volumetric rate drops and the interface moves upwards inside the cold leg pipe. It is assumed and observed that the Kelvin Helmholtz instabilities enhance the mixing rate. It is also assumed that the mixing rate approaches asymptotically to a diffusion/convective limit (i.e. a ceases to be a function of fluid velocity). Future work can include analyzing the moment this limit is achieved as the velocities go to zero or drop below a critical value when the interface assumes a wave pattern. It was observed that after a long period of time, in the order of hours, the fluids in the tank and annulus remain stratified while fluid inside the cold-leg becomes fully mixed.



Figure 8.1: End of Mixing.



It is worth noting that the Open Test working fluids presented fewer complications than the Blind Test fluids during the experiment. That is because due to the higher concentration of ethanol in the BT light fluid, entrapment of air and consequent micro bubble formation created a challenge when performing PIV and LIF measurements. This effect can be observed in figure 6.10. The bubbles that are formed on the top wall surface obscured the field of vision in the visualization window while also obstructing the laser sheet, thus creating streaks of shadows that disrupted the capturing of information over the area. Reflections also presented a challenge for both OT and BT. Future work can work towards utilizing different methods that can reduce the reflections and bubble formation. Other future work includes,

- Taking measurements of axial pressure along the vessel/barrel wall.
- Applying LIF technique within the downcomer region.
- PIV measurements in the lower plenum and core plate.
- Perform measurements to further investigate fluid properties (i.e. Diffusivity) .

The Open Test and the Blind Test demonstrated similar trends in the analysis of the data collected. This set of experiments will help take a step closer to the validation of CFD simulations performed that seek to study mixing/buoyancy driven flow to test nuclear reactor safety of a Pressurized Water Reactor.

## REFERENCES

- [1] *Particle Image Velocimetry*. Cambridge Aerospace Series, 2010.
- [2] *Laser Chemistry: Spectroscopy, Dynamics and Applications*. Wiley, 2007.
- [3] B. J Kim, Y. Liu, and H. J. Sung, “Micro piv measurement of two-fluid flow with different refractive indices,” *Measurement Science & Technology - MEAS SCI TECHNOL*, vol. 15, pp. 1097–1103, 06 2004.
- [4] U. Rohde, S. Kliem, T. Höhne, R. Karlsson, B. Hemström, J. Lillington, T. Toppila, J. Elter, and Y. Bezrukov, “Fluid mixing and flow distribution in the reactor circuit, measurement data base,” *Nuclear Engineering and Design*, vol. 235, pp. 421–443, 02 2005.
- [5] H. D. Kweon, J. S. Kim, and K. Y. Lee, “Fatigue design of nuclear class 1 piping considering thermal stratification,” *Nuclear Engineering and Design*, vol. 238, no. 6, pp. 1265 – 1274, 2008.
- [6] E. Eggertson, R. Kapulla, J. Fokken, and H. Prasser, “Turbulent mixing and its effects on thermal fatigue in nuclear reactors,” *World Academy of Science, Engineering and Technology*, vol. 76, pp. 206–213, 04 2011.
- [7] I. Farkas, E. Hutli, T. Farkas, A. Takács, A. Guba, and I. Tóth, “Validation of computational fluid dynamics calculation using rossendorf coolant mixing model flow measurements in primary loop of coolant in a pressurized water reactor model,” *Nuclear Engineering and Technology*, vol. 48, no. 4, pp. 941 – 951, 2016.
- [8] S. Kliem, T. Höhne, U. Rohde, and F.-P. Weiss, “Experiments on slug mixing under natural circulation conditions at the rocom test facility using high-resolution measurement techniques and numerical modeling,” *Nuclear Engineering and Design*, vol. 240, pp. 2271–2280, 09 2010.

- [9] C. Härtel and F. NECKER, “Analysis and direct numerical simulation of the flow at a gravity-current head. part 1. flow topology and front speed for slip and no-slip boundaries,” *Journal of Fluid Mechanics*, vol. 418, pp. 189 – 212, 09 2000.
- [10] V. Chudanov, A. V. Obabko, P. Fischer, T. Tautges, V. Goloviznin, M. A. Zaytsev, V. A. Perovichko, A. Aksenova, and S. Karabasov, *Large Eddy Simulation of Thermo-Hydraulic Mixing in a T-Junction*. 02 2013.
- [11] K. A. J. W. LB.L. Smith, J.H. Mahaffy, “Report of the oecd/nea-vattenfall t-junction benchmark exercise,” tech. rep., Report of the OECD/NEA-Vattenfall T-Junction Benchmark exercise, 2011.
- [12] T. Frank, S. Jain, A. A Matyushenko, and A. Garbaruk, “The oecd/nea matis-h benchmark - cfd analysis of water flow through a 5x5 rod bundle with spacer grids using ansys fluent and ansys cfx,” 09 2012.
- [13] R. , J. Travis, B. , and J. Kim, “Gas flow validation tests with panda from the oecd seth benchmark covering steam / air and steam / helium / air mixtures,” 09 2008.
- [14] A. Krueger, F. Sarikurt, L. Carasik, and Y. Hassan, “Uncertainty quantification by monte carlo analysis using cfd simulations for gemix benchmark activities,” 11 2016.
- [15] T. Höhne, S. Kliem, and U. Bieder, “Iaea crp benchmark of rocom pts test case for the use of cfd in reactor design using the cfd-codes ansys cfx and triocfd,” *Nuclear Engineering and Design*, vol. 333, pp. 161–180, 07 2018.
- [16] M. Loginov, E. Komen, and A. Kuczaj, “Application of large-eddy simulation to pressurized thermal shock problem: A grid resolution study,” *Nuclear Engineering and Design - NUCL ENG DES*, vol. 240, pp. 2034–2045, 08 2010.
- [17] Q. , U. Bieder, and T. Höhne, “Analysis of buoyancy-driven flow in the rocom test facility,” 07 2016.
- [18] B. Krohn, S. Qin, A. Manera, and V. Petrov, “Refractive index matching for optical flow investigation with high density stratification,” 07 2018.

- [19] T. Nguyen, N. Goth, P. Jones, S. Lee, R. Vaghetto, and Y. Hassan, “Piv measurements of turbulent flows in a 61-pin wire-wrapped hexagonal fuel bundle,” *International Journal of Heat and Fluid Flow*, vol. 65, pp. 47–59, 03 2017.
- [20] A. Eckstein and P. P. Vlachos, “Digital particle image velocimetry (dpiv) robust phase correlation,” *Measurement Science and Technology*, vol. 20, p. 055401, apr 2009.
- [21] M. Raffel, C. Willert, and J. Kompenhans, *Particle Image Velocimetry: A Practical Guide*. 01 1998.
- [22] J. Westerweel, “Efficient detection of spurious vectors in particle image velocimetry data,” *Experiments in Fluids*, vol. 16, pp. 236–247, 02 1994.
- [23] B. Pérez Díaz, S. Castanedo, and P. Palomar, “Experimental characterization of saline density currents generated by brine discharges,” 05 2016.
- [24] P. Odier, J. Chen, and R. Ecke, “Entrainment and mixing in a laboratory model of oceanic overflow,” *Journal of Fluid Mechanics*, vol. 746, 04 2014.
- [25] D. Xu and J. Chen, “Experimental study of stratified jet by simultaneous measurements of velocity and density fields,” *Experiments in Fluids*, vol. 53, 07 2012.
- [26] T. Brooke Benjamin, “Gravity currents and related phenomena,” *Journal of Fluid Mechanics*, vol. 31, pp. 209 – 248, 01 1968.
- [27] J. L. Hartley, “Double ended guillotine break in a prismatic block vhr lower plenum air ingress scenario,” Master’s thesis, Texas A&M University, 2011.
- [28] H. Lemonnier and D. Lakehal, “Test-case no 28: The lock-exchange flow(n, pa),” *Multiphase Science and Technology*, vol. 16, pp. 171–175, 01 2004.
- [29] “Uncertainty analysis particle imaging velocimetry,” tech. rep., International Towing Tank Conference, 2008.

- [30] B. H. Timmins, B. W. Wilson, B. L. Smith, and P. P. Vlachos, “A method for automatic estimation of instantaneous local uncertainty in particle image velocimetry measurements,” *Experiments in Fluids*, vol. 53, pp. 1133–1147, Oct 2012.
- [31] B. Wilson and B. Smith, “Uncertainty on piv mean and fluctuating velocity due to bias and random errors,” *Measurement Science and Technology*, vol. 24, p. 035302, 02 2013.
- [32] F. Gavelli and K. Kiger, “Experimental investigation of liquid mixing in a complex annular geometry,” 11 1998.

APPENDIX A

TAMU-PTSUQ-VOT-001-REV0



## TECHNICAL DOCUMENT COVER PAGE

Document No:	TAMU-PTSUQ-VOT-001	Revision: 0	Page 1 of 9
		Date: 10/18/2017	
Doc Title:	Isolation Valve Opening Time		
Project Name:	Cold Leg Mixing CFD-UQ Benchmark		
Document Purpose/Summary:			
This document provides the isolation valve opening time data			
Total Page Count: 9 pages.			




## TECHNICAL DOCUMENT COVER PAGE

Document No:	TAMU-PTSUQ-DWG-001	Revision: 0	Page 2 of 9
Doc Title:	Experimental Facility CAD Drawings		


Prepared by:	Vasileios Kyriakopoulos
	Daniel Orea
Reviewed by:	Rodolfo Vaghetto
	Thien Nguyen



	Isolation Valve Opening Time		
	Document No: TAMU-PTSUQ-VOT-001	Rev: 0	Page 3 of 9


Document Number: TAMU-PTSUQ-VOT-001 Revision: 0

REVISION	DATE	DESCRIPTION
0	10/18/2017	First release

	Isolation Valve Opening Time		
	Document No: TAMU-PTSUQ-VOT-001	Rev: 0	Page 4 of 9

## TABLE OF CONTENTS

TABLE OF CONTENTS.....	54
1.0 SCOPE .....	55
2.0 VALVE GEOMETRY .....	55
3.0 VALVE OPENING TIME.....	56

	Isolation Valve Opening Time		
	Document No: TAMU-PTSUQ-VOT-001	Rev: 0	Page 5 of 9

**1.0 SCOPE**

This document provides the opening time of the isolation valve installed in the cold leg of the “Cold Leg Mixing” experimental facility, providing a general description of the methodology adopted for the estimation.

**2.0 VALVE GEOMETRY**

The isolation valve is installed on the cold leg pipe and kept closed during the test preparation to keep the working fluids separated. When the test is initiated, the valve is opened to allow mixing of the two fluids.

Details on dimensions of the valve can be found in the facility drawings (TAMU-PTSUQ-DWG-001). The valve is connected to an opening mechanism with spring to allow for fast opening times. When closed, the spring is in tension and the mechanism is hold in place by a bolt lock. To open the valve, the bolt lock is removed, the lever is released and the spring pulls on the lever which in turn pulls the stem of the valve gate. The valve is connected on both sides to a 2” (nominal ID) acrylic legs as shown in **Figure 2-1** and **Figure 2-2**.

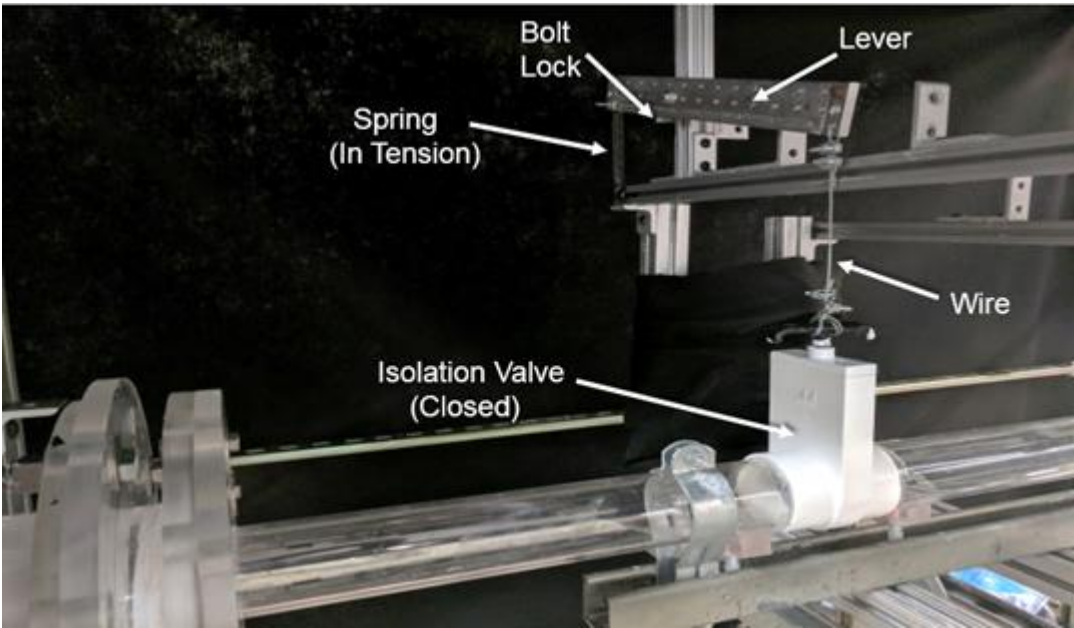


**Figure 2-1 Valve and opening mechanism (Fully-Closed Position)**

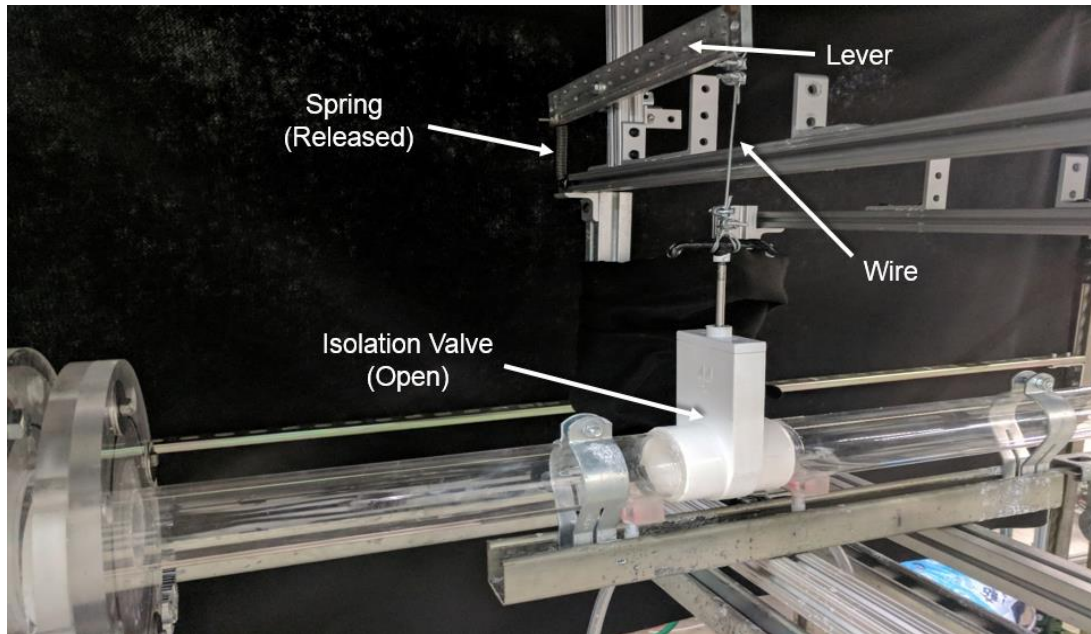


**Figure 2-2 Valve and opening mechanism (Fully-Open Position)**

### 3.0 VALVE OPENING TIME

The valve opening time is estimated by post-processing a video taken with a high-speed camera placed in front of the valve, facing the valve gate. The video is recorded with a frame rate of 5000 fps. The test is repeated five times to account for test repeatability.

**Figure 3-1** to **Figure 3-4** show selected snapshots of the video recorded at different valve gate positions: The snapshot named “**Point\_1**” shows the valve gate at its fully closed position, which corresponds to a time  $t < 0$  prior the reference time of  $t = 0$ s. After the bolt is released, the valve gate starts moving upward while the active flow area is still zero<sup>1</sup>. The reference time ( $t = 0$ s) is assumed to be the time at which the active flow area starts increasing from zero. The snapshot named “**Point\_2**” is taken at  $t = 0$ s. The snapshot named “**Point\_3**” is taken when the valve gate has moved half-way upwards. The snapshot named “**Point\_4**” is taken when the valve reaches its fully open position.

---

<sup>1</sup> This is due to the design features of the valve gate (refer to drawings document TAMU-PTSUQ-DWG-001)

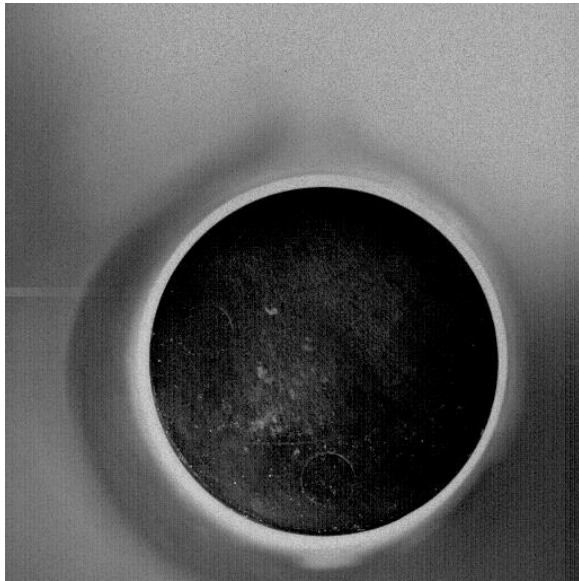


Figure 3-1 Point\_1 Valve completely closed

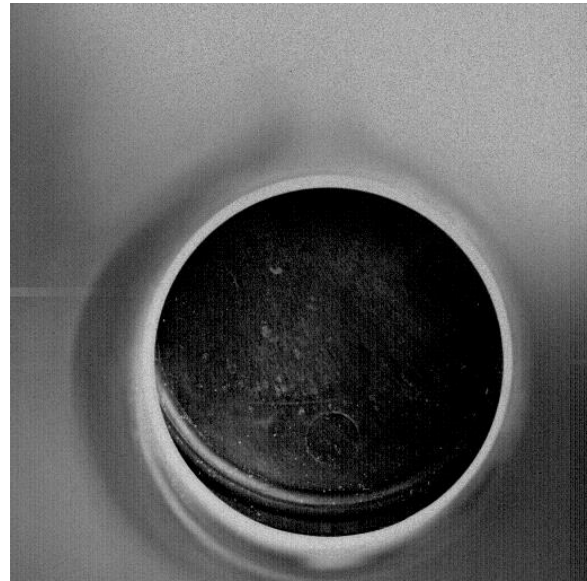


Figure 3-2 Point\_2 Valve gate at  $t=0$ sec

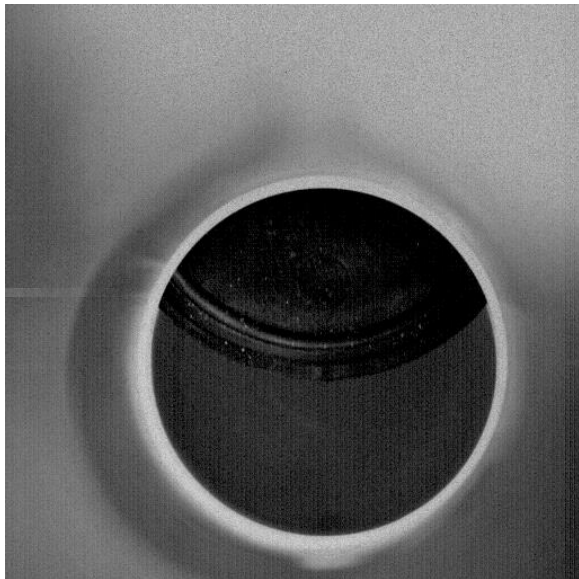


Figure 3-3 Point\_3 Valve gate half-way

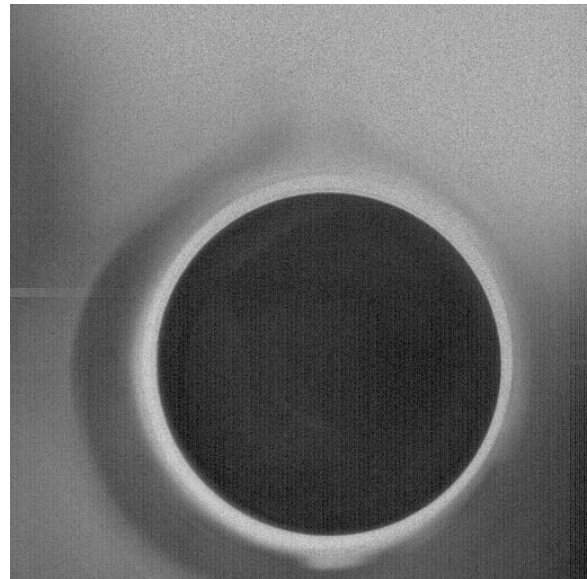


Figure 3-6 Point\_4 Valve completely open



Figure 3-5 shows the normalized flow area<sup>2</sup> as function of time for all five data sets. The data are plotted from the time  $t=0s$  described above. Data average and error ( $\pm 2\sigma$  of the measurements) are also shown as well as a fit curve for the average normalized area.

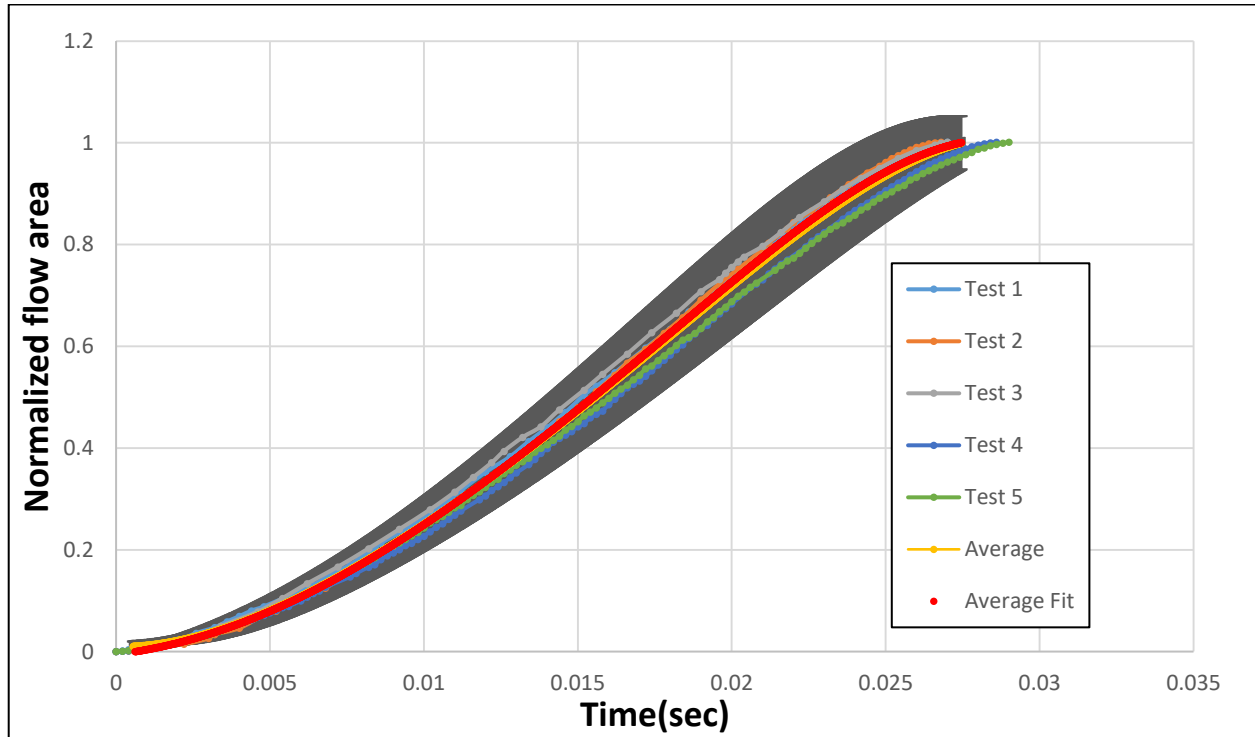


Figure 3-5 Normalized flow area<sup>2</sup> Vs time

The equation for the fit curve is given by:

$$A_{norm}(t) = a1 * \sin(b1 * t + c1) + a2 * \sin(b2 * t + c2) + a3 * \sin(b3 * t + c3) \quad (1)$$


where

$$a1 = 1.507, b1 = 102.3, c1 = 0.08647, a2 = 7.074, b2 = 155, c2 = 3.027, a3 = 5.957,$$

$$b3 = 160.4, c3 = 6.124$$

---

<sup>2</sup> Area normalized to the total flow area of the valve calculated from the pictures post processing = 2120.298432mm<sup>2</sup>

	Isolation Valve Opening Time		
	Document No: TAMU-PTSUQ-VOT-001	Rev: 0	Page 9 of 9

The Root Mean Square Error (RMSE) is:

$$\text{RMSE} = 0.00113 \quad (2)$$

The average valve opening time<sup>3</sup> is:

$$t_{open}^{ave} = 0.02768s \quad (3)$$

---

<sup>3</sup> From the reference time (t=0s) to full open position.

APPENDIX B

TAMU-PTSUQ-DWG-001-REV0





## TECHNICAL DOCUMENT COVER PAGE

Document No:	TAMU-PTSUQ-DWG-001	Revision: 0	Page 1 of 8
		Date: 10/19/2017	
Doc Title:	Experimental Facility CAD Drawings		
Project Name:	Cold Leg Mixing CFD-UQ Benchmark		
Document Purpose/Summary:			
This document provides an overview of the experimental facility. CAD drawings are included as electronic attachment			
Total Page Count: 9 pages.			




## TECHNICAL DOCUMENT COVER PAGE

Document No:	TAMU-PTSUQ-DWG-001	Revision: 0	Page 2 of 8
Doc Title:	Experimental Facility CAD Drawings		


Prepared by:	Blake Maher
	Daniel Orea
	Rodolfo Vaghetto
Reviewed by:	Giacomo Busco
	Jonathan Lai
	Thien Nguyen

## REVISION HISTORY LOG

	Experimental Facility CAD Drawings		
	Document No: TAMU-PTSUQ-DWG-001	Rev: 0	Page 3 of 8


Document Number: TAMU-PTSUQ-DWG-001 Revision: 0

REVISION	DATE	DESCRIPTION
0	10/19/2017	First release

	Experimental Facility CAD Drawings		
	Document No: TAMU-PTSUQ-DWG-001	Rev: 0	Page 4 of 8

## TABLE OF CONTENTS

TABLE OF CONTENTS.....	64
1.0 SCOPE.....	65
2.0 EXPERIMENTAL FACILITY OVERVIEW.....	65
3.0 FACILITY DRAWINGS.....	66
3.1 Notes to the Analysts.....	67
ATTACHMENT I – DRAWINGS.....	68

	Experimental Facility CAD Drawings		
	Document No: TAMU-PTSUQ-DWG-001	Rev: 0	Page 5 of 8

## 1.0 SCOPE

This document is prepared to provide a general overview of the experimental facility. The document contains the CAD drawings of the facility as electronic attachment.

## 2.0 EXPERIMENTAL FACILITY OVERVIEW

An overview of the experimental setup is shown in Figure 2-1. The facility of two cylindrical vessels connected through a circular pipe. The following components are included in the facility:

- The Reactor vessel (right), with an internal cylindrical pipe to simulate the reactor barrel, and the downcomer, delimited by the inner surface of the reactor vessel and the outer surface of the barrel.
- The reservoir (left) where heavy fluid is stored at the beginning of the test
- The cold leg, connecting the reactor vessel with the reservoir, with the isolation valve.

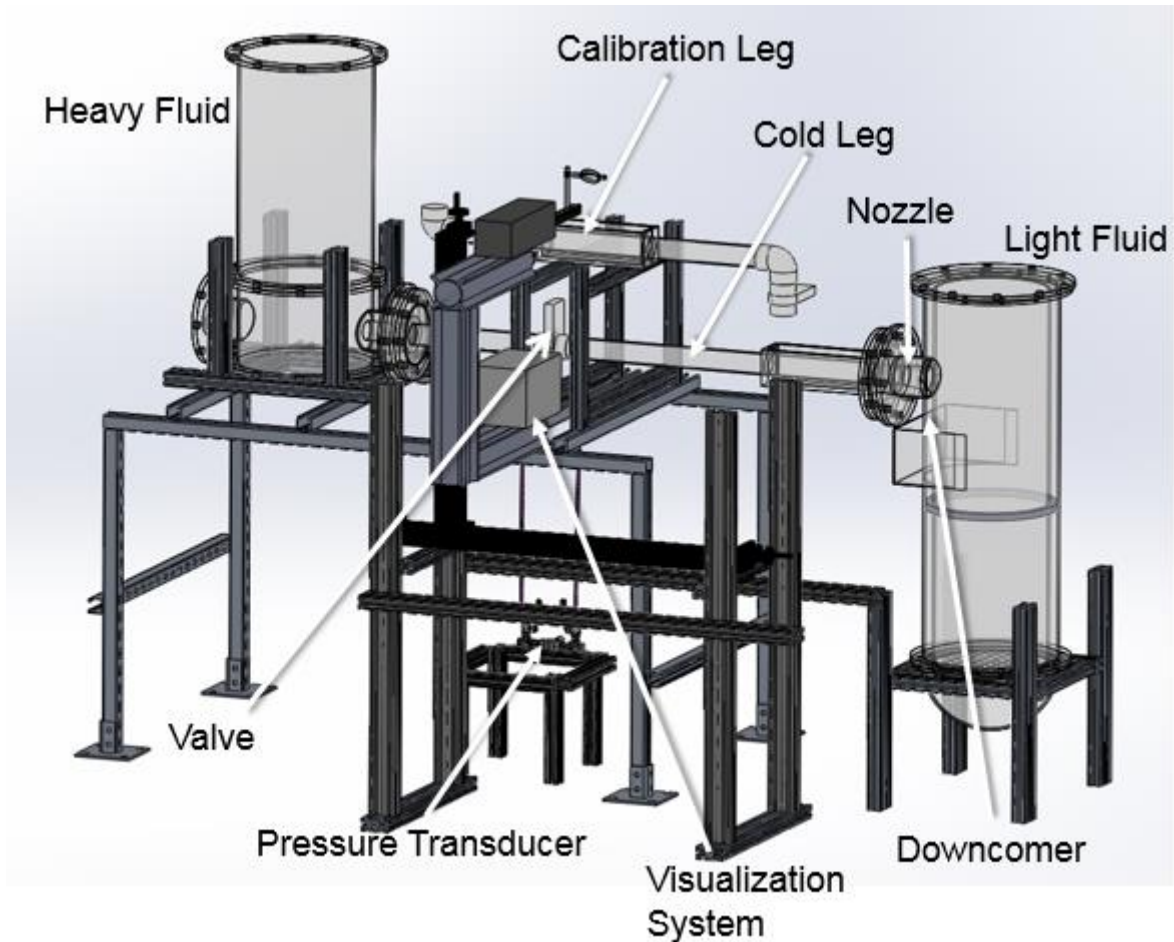



**Figure 2-1. Facility Overview**

The cold leg is connected to the reactor vessel through a vessel nozzle. Transparent acrylic is used to fabricate the majority of the components of the facility to allow flow visualization and measurements of the parameters of interest.

### **3.0 FACILITY DRAWINGS**

The drawings of the experimental facility are prepared using SolidWorks® software. The drawings are included as electronic attachment. The drawings include only the fluid domain of the facility. Instrumentation, support structures, and other external components are not included in the drawings.

The experimental facility has been modified to facilitate the test preparation procedures, by reducing the total volume of the reactor vessel. The drawings reflect the current status of the facility and include such modifications.

	Experimental Facility CAD Drawings		
	Document No: TAMU-PTSUQ-DWG-001	Rev: 0	Page 7 of 8

An isometric view of the current fluid domain of the facility that will be used for the test activity is shown in Figure 3-1.

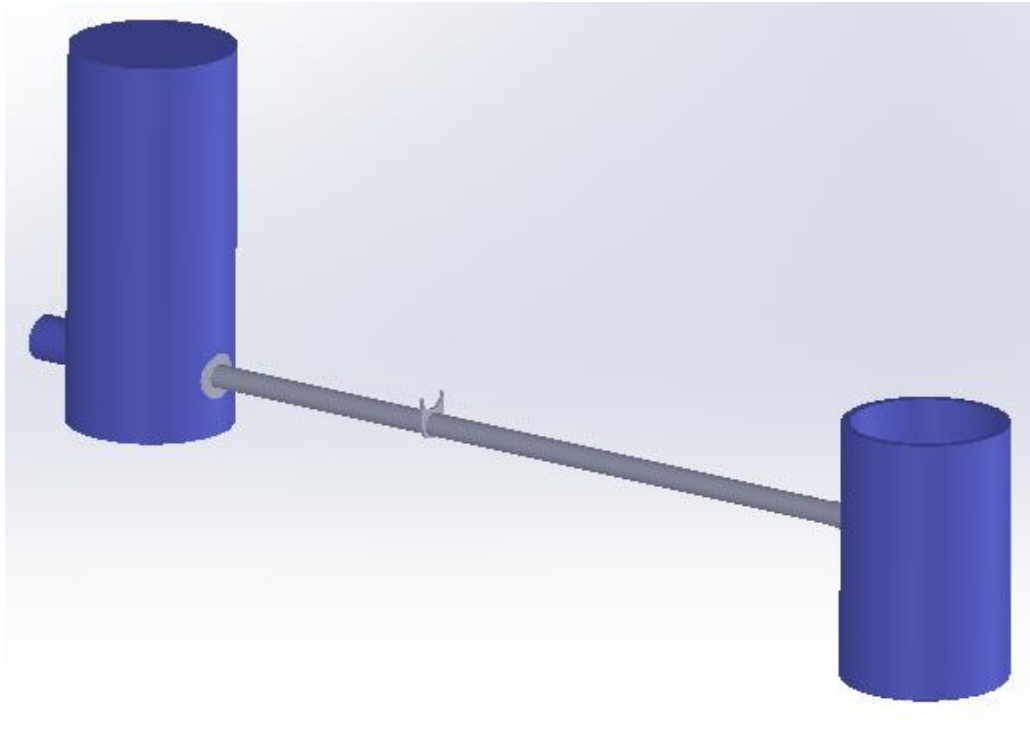



**Figure 3-1. Isometric View of the Facility Fluid Domain**

### **3.1 Notes to the Analysts**

The liquid level of the heavy fluid in the reservoir is defined as boundary condition at the beginning of each test. Please refer to the test boundary conditions to impose the initial level of the heavy fluid in the reservoir.

The liquid level of the light solution in the reactor vessel corresponds to the top of the vessel for every test. Please refer to the test boundary conditions for additional information on the initial liquid level in the reactor vessel.

The inner volume of the reactor barrel (inner cylinder) is empty and no flow is allowed for the downcomer to the inner side of the barrel.

	Experimental Facility CAD Drawings		
	Document No: TAMU-PTSUQ-DWG-001	Rev: 0	Page 8 of 8

Detailed drawings of the isolation valve component are also included in the drawings, as well as the location of the pressure taps across the valve.

## **ATTACHMENT I – DRAWINGS**

Attachment list

TAMU-PTSUQ-DWG-001-rev0.zip



APPENDIX C

TAMU-PTSUQ-OCB-001-REV0



## TECHNICAL DOCUMENT COVER PAGE

TAMU-PTSUQ-OCB-001	Revision: 0	Page 1 of 9
	Date: 11/13/2017	
Doc Title: Boundary Conditions - <b>Target: Open Test</b>		
Project Name: Cold Leg Mixing CFD-UQ Benchmark		
Document Purpose/Summary:  This document provides a description of the target boundary conditions applied to the open test.  Total Page Count: 9 pages.		




## TECHNICAL DOCUMENT COVER PAGE

Document No:	TAMU-PTSUQ-OCB-001	Revision: 0	Page 2 of 9
Doc Title:	Boundary Conditions - Target: Open Test		


Prepared by:	Daniel Orea
	Rodolfo Vaghetto
Reviewed by:	Thien Nguyen
	Yassin Hassan

# REVISION HISTORY LOG

	Boundary Conditions - Target: Open Test		
	Document No: TAMU-PTSUQ-OCB-001	Rev: 0	Page 3 of 9

Document Number: TAMU-PTSUQ-OCB-001 Revision: 0

REVISION	DATE	DESCRIPTION
0	11/13/2017	First release

	Boundary Conditions - Target: Open Test		
	Document No: TAMU-PTSUQ-OCB-001	Rev: 0	Page 4 of 9

## TABLE OF CONTENTS

TABLE OF CONTENTS .....	4
DEFINITIONS AND ACRONYMS.....	5
1.0 SUMMARY AND SCOPE .....	6
2.0 WORKING FLUIDS SELECTION .....	6
3.0 BOUNDARY CONDITIONS .....	6
3.1 Density.....	6
3.1.1 Heavy Fluid Density .....	7
3.1.2 Light Fluid Density .....	7
3.1.3 Density Difference.....	7
3.2 Viscosity .....	7
3.2.1 Heavy Fluid Viscosity.....	7
3.2.2 Light Fluid Viscosity .....	7
4.0 INITIAL CONDITIONS.....	8
5.0 FINAL REMARKS .....	9



## DEFINITIONS AND ACRONYMS

DI	De-Ionized
H	Heavy
L	Light



## 1.0 SUMMARY AND SCOPE

This document is prepared to provide the targeted boundary and initial conditions for the open test. The target boundary and initial conditions are provided to the analysts to perform pre-test simulations.

Actual boundary and initial conditions for the open test will be evaluated and measured at the time of test execution.

The following conditions are described in this

document: Boundary Conditions

- Working Fluids Density
- Working Fluids Viscosity
- Density Difference

Initial Conditions (Before Valve Opening)

- Heavy fluid liquid level

## 2.0 WORKING FLUIDS SELECTION

The following fluids are selected for the open

test: Heavy Density Fluid

Low Density Fluid

Fluid properties are described in Section 3.0 (Boundary Conditions)

## 3.0 BOUNDARY CONDITIONS

Density and viscosity of the selected working fluids are measured at the beginning of each test. The values reported in the following sections are targeted values.

### 3.1 Density

Densities are estimated by measuring the mass of a 10-ml sample taken from batch of solution maintained at a given temperature (Volume accuracy =  $\pm 0.055$  ml; Mass accuracy =  $\pm 0.0001$  g).



### 3.1.1 Heavy Fluid Density

The density of the heavy (H) fluid is:

$$\rho_H = 1074.4 \text{ kg/m}^{31}$$

### 3.1.2 Light Fluid Density

The density of the light (L) fluid is:

$$\rho_L = 963.22 \text{ kg/m}^{32}$$

### 3.1.3 Density Difference

The density difference achieved with the selected heavy and light fluids is:

$$\Delta\rho = \rho_H - \rho_L = 111.18 \text{ kg/m}^3$$

## 3.2 Viscosity

Viscosity is measured at  $22.4 \text{ }^\circ\text{C} \pm 0.1 \text{ }^\circ\text{C}$

### 3.2.1 Heavy Fluid Viscosity

The viscosity of heavy (H) fluid is:

$$\mu_H = 0.0011354 \text{ Pa} \cdot \text{s} \pm 1.5\%$$

### 3.2.2 Light Fluid Viscosity

The viscosity of the light (L) fluid is:

$$\mu_L = 0.0022733 \text{ Pa} \cdot \text{s} \pm 1.5\%$$

---

<sup>1</sup> Average based on 10 samples, with standard deviation of  $\sigma_H = 24.73 \text{ kg/m}^3$

<sup>2</sup> Average based on 10 samples, with standard deviation of  $\sigma_L = 21.65 \text{ kg/m}^3$





#### 4.0 INITIAL CONDITIONS

The initial conditions refer to the status of the liquid levels in the test facility at the time the test is initiated, which corresponds to the time the isolation valve is open.

When preparing the test, the light side of the facility will be filled with light fluid up to the top of the vessel as shown in Figure 4-1 (levels are referred to the cold leg centerline).

The level of the light fluid correspond to the height of the reactor vessel (Figure 4-1, right), equal to:

$$H_L = 27.9 \text{ cm}$$

The level of the heavy fluid (Figure 4-1, left) is calculate from the densities of the fluids reported in Section 3.1, in order to equalize the pressure across the isolation valve at the test start.

$$H_H = \frac{\rho_L}{\rho_H} H_L = 25.0 \text{ cm}$$

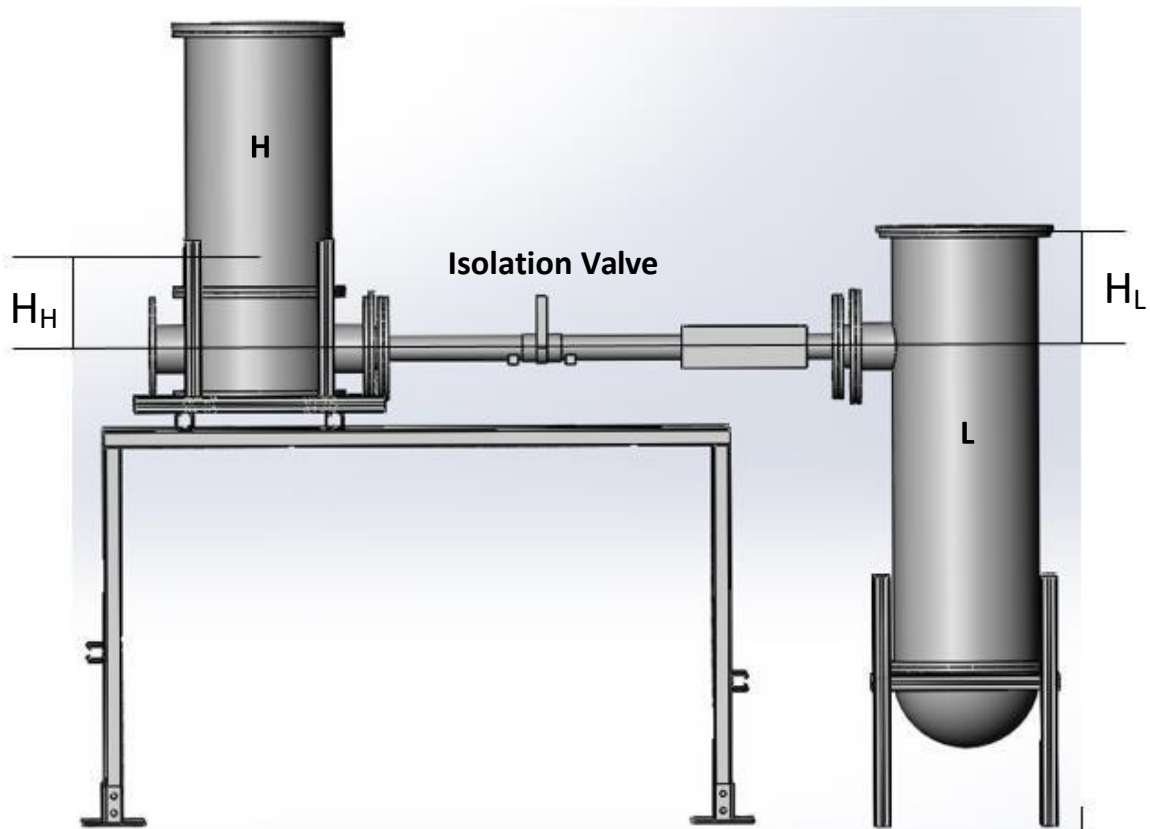



Figure 4-1. Liquid Levels

	Boundary Conditions - Target: Open Test		
	Document No: TAMU-PTSUQ-OCB-001	Rev: 0	Page 9 of 9

**5.0 FINAL REMARKS**

Actual density of heavy and light solutions will be evaluated at the time of the test execution.  
Temperature of the solutions will be monitored and recorded during the test.

APPENDIX D

TAMU-PTSUQ-OT3-REV1.1



## TECHNICAL DOCUMENT COVER PAGE

Document No:	TAMU-PTSUQ-OT3	Revision: 1.1	Page 1 of 13
Doc Title:	Cold Leg Mixing CFD-UQ Benchmark Open Test		
Project Name:	Cold Leg Mixing CFD-UQ Benchmark		
<p>Document Purpose/Summary: This document provides a summary of the data collected for the first open test of the Cold Leg Mixing CFD-UQ Benchmark.</p> <p>Total Page Count: 13 pages.</p>			




## TECHNICAL DOCUMENT COVER PAGE


Document No:	TAMU-PTSUQ-OT3	Revision: 1.1	Page 2 of 13

Prepared by:	Daniel Orea
	Vasileios Kyriakopoulos
Reviewed by:	Rodolfo Vaghetto
	Thien Nguyen
	Yassin Hassan

## REVISION HISTORY LOG


	TAMU Pressurized Thermal Shock Open Test Summary		
	Document No: TAMU-PTSUQ-OT3	Rev: 1.1	Page 3 of 13

REVISION	DATE	DESCRIPTION
0	02/04/18	First Release
1	02/22/2018	Origin of the coordinate system for Cold-Leg and Downcomer data updated (Section 3.1, Section 3.2). Included time-averaged velocities and Reynold stresses for 10-second intervals for both the Cold Leg and Downcomer (See Tables 2 and 4)
1.1	03/01/2018	Added definition of the Standard Deviation (Section 4.0) Added a time-averaged velocities and Reynold stresses for downcomer. (See Table 4)

	TAMU Pressurized Thermal Shock Open Test Summary		
	Document No: TAMU-PTSUQ-OT3	Rev: 1.1	Page 4 of 13

## Table of Contents

Acronyms and Definitions .....	84
1.0 Scope .....	85
2.0 Initial Conditions .....	85
2.1 Temperature .....	86
3.0 Velocity Measurement Locations.....	86
3.1 Cold Leg Velocity Measurements .....	87
3.2 Downcomer Velocity Measurements .....	88
4.0 Description of Data Sets.....	89
4.1 Cold-Leg Data Sets.....	89
4.2 Downcomer Data Sets.....	90
5.0 Electronic Attachments .....	92

	TAMU Pressurized Thermal Shock Open Test Summary		
	Document No: TAMU-PTSUQ-OT3	Rev: 1.1	Page 5 of 13

## ACRONYMS AND DEFINITIONS

$H_H$  – Height of Heavy Fluid

$H_L$  – Height of Light Fluid

$\rho_H$  - Heavy Fluid Density


$\rho_L$  - Light Fluid Density

$\mu_H$  - Heavy Fluid Viscosity

$\mu_L$  - Light Fluid Viscosity

sd – Standard Deviation



	TAMU Pressurized Thermal Shock Open Test Summary		
	Document No: TAMU-PTSUQ-OT3	Rev: 1.1	Page 6 of 13

## 1.0 SCOPE

This document provides information about the experimental data sets collected for the first open test of the Cold Leg Mixing CFD-UQ Benchmark. The data sets contain the velocity measurements, along with the particle image velocimetry (PIV) statistical analysis.

## 2.0 INTIAL CONDITIONS

The density and viscosity of the light and heavy solutions used during the test are reported below.


- Density
  - $\rho_H = 1064.7 \text{ kg/m}^3$
  - $\rho_L = 956.54 \frac{\text{kg}}{\text{m}^3}$
- Viscosity
  - $\mu_H = 0.00109 \text{ Pa} \cdot \text{s}$
  - $\mu_L = 0.00245 \text{ Pa} \cdot \text{s}$

The level of the light fluid (Figure1, right) corresponds to the height of the reactor vessel measured from the center-line of the leg, which is equal to:

$$H_L = 27.9 \text{ cm}$$

The level of the heavy fluid (Figure 1, left) is calculated from the densities of the fluids reported above, in order to equalize the pressure across the isolation valve at the start of the test.

$$H_H = \frac{\rho_L}{\rho_H} H_L = 25.06 \text{ cm}$$

	TAMU Pressurized Thermal Shock Open Test Summary		
	Document No: TAMU-PTSUQ-OT3	Rev: 1.1	Page 7 of 13

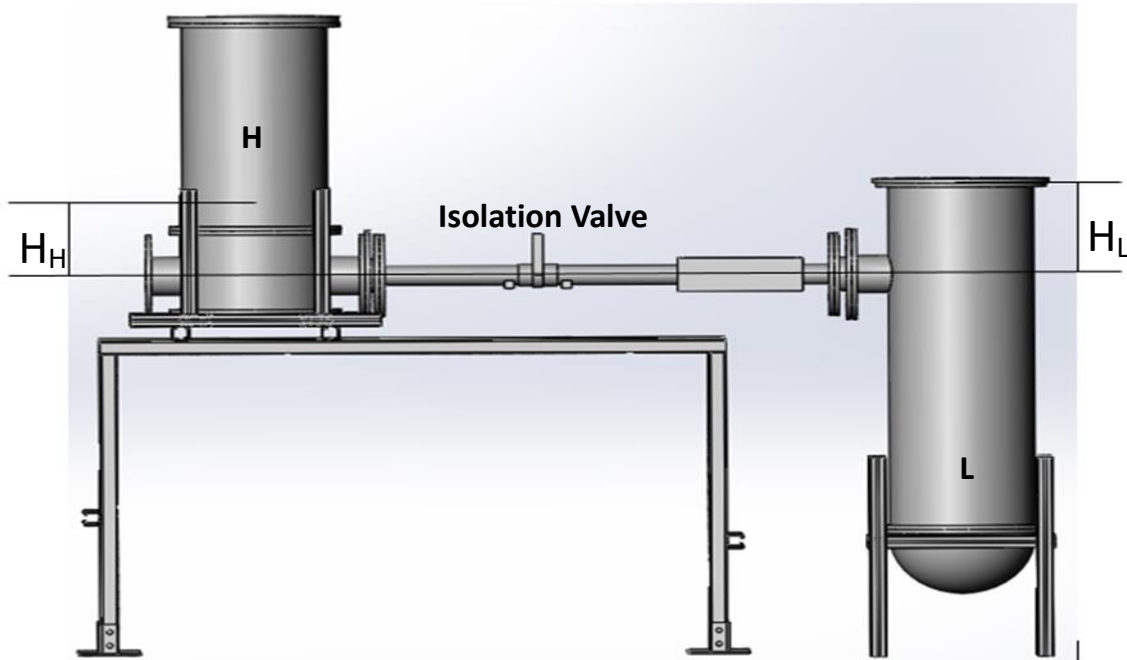


**Figure 1. Liquid Levels**

An overview of the facility can be found in the facility drawings (TAMU-PTSUQ-DWG-001).

A detailed explanation of the valve opening time can be found in isolation valve document (TAMU-PTSUQ-VOT-001).


## 2.1 Temperature

A constant ambient temperature of  $20.5\text{ }^{\circ}\text{C} \pm 0.3\text{ }^{\circ}\text{C}$  was measured in both fluids and maintained for the duration of the experiment.

## 3.0 VELOCITY MEASUREMENT LOCATIONS

Velocity was recorded at two locations when performing the test, as shown in Figure 2 and 3:

- Cold Leg
- Downcomer

	TAMU Pressurized Thermal Shock Open Test Summary		
	Document No: TAMU-PTSUQ-OT3	Rev: 1.1	Page 8 of 13

### 3.1 Cold Leg Velocity Measurements

The location of the origin for the cold-leg measurement window is selected as follows:

- $x = 0$  at 69.56 cm from the mid-plane of the valve, as shown in Figure 2.
- $y = 0$  at 3.03 cm below the center-line for the leg.
- $z = 0$  at center-plane of the leg

The positive direction of each axis is also shown in Figure 2.


The minimum and maximum X-Y coordinates of the measurement region are (Figure 2, zoom):

- $X_{\min} = 0.111$  cm;  $X_{\max} = 17.67$  cm
- $Y_{\min} = 0.111$  cm;  $Y_{\max} = 5.67$  cm.

The x-y plane is located at the mid-plane of the leg, parallel to the center-line.

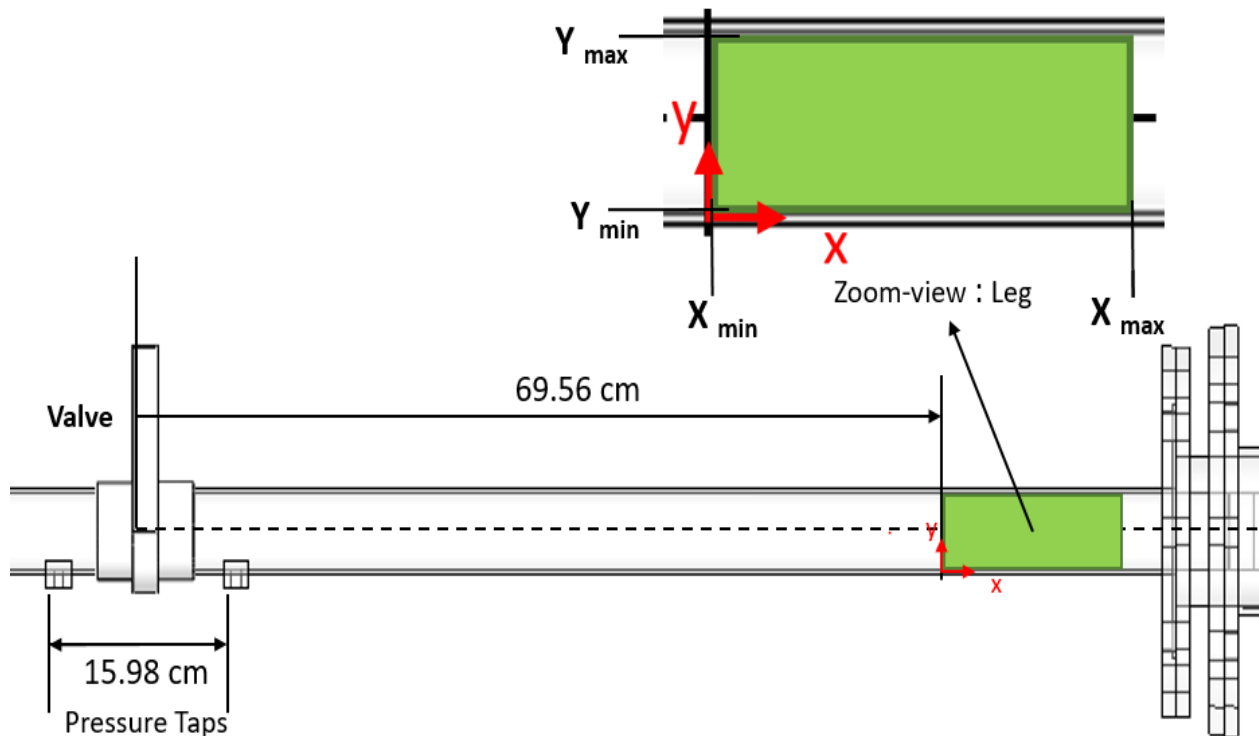


**Figure 2: Measurement Location**

	TAMU Pressurized Thermal Shock Open Test Summary		
	Document No: TAMU-PTSUQ-OT3	Rev: 1.1	Page 9 of 13

### 3.2 Downcomer Velocity Measurements

The location of the origin for the downcomer measurement window is selected as follows:

- $x = 0$  at 14.5 cm from the center-line of the nozzle, as shown in Figure 3.
- $y = 0$  at 0.219 cm from the inside inner-wall of the vessel, as shown in Figure 3.
- $z = 0$  at the vertical mid-plane of the vessel.

The positive direction of each axis is also shown in Figure 3.


The minimum and maximum X-Y coordinates of the measurement region are:

- $X_{\min} = 0.050$  cm;  $X_{\max} = 2.35$  cm
- $Y_{\min} = 0.050$  cm;  $Y_{\max} = 7.97$  cm.

The x-y plane is location shown in Figure 3.

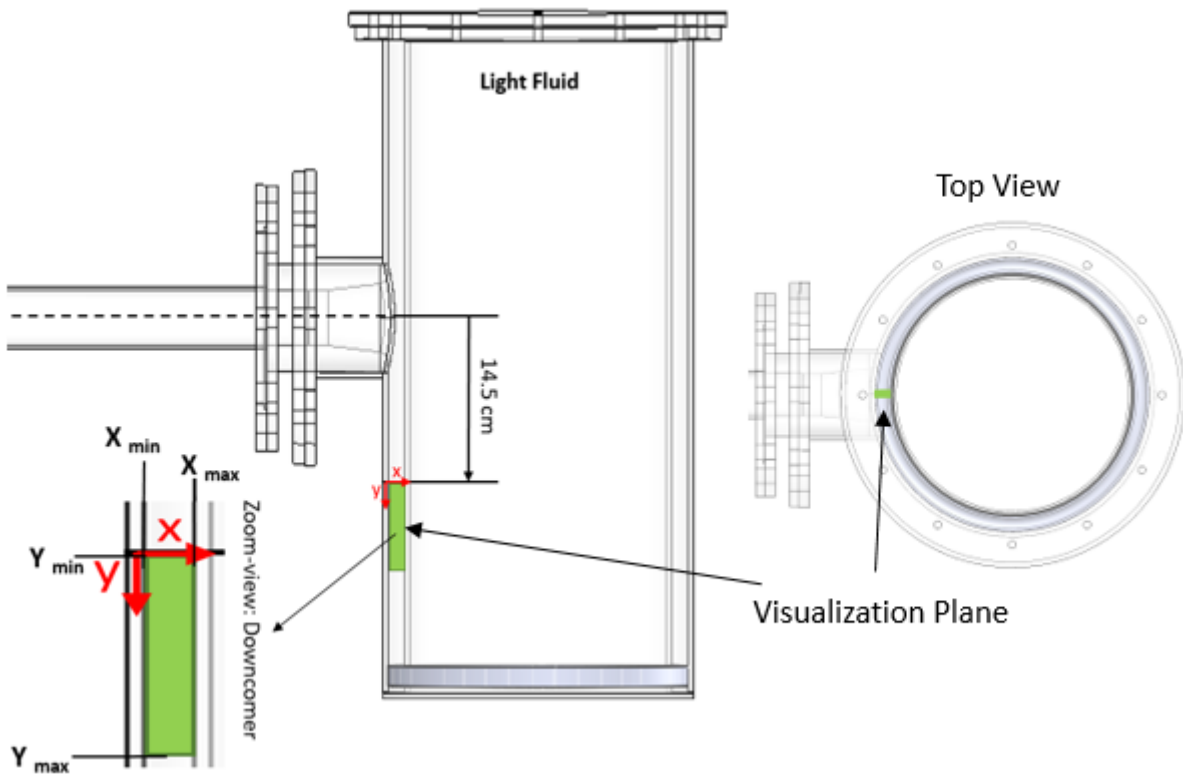


**Figure 3: Measurement Location**

	TAMU Pressurized Thermal Shock Open Test Summary		
	Document No: TAMU-PTSUQ-OT3	Rev: 1.1	Page 10 of 13

#### 4.0 DESCRIPTION OF DATA SETS

This section provides information on the contents of the .txt files containing the experimental data. A list of electronic attachments is included in Section 5.0.

The structure for each .txt file is described in the following tables.

**Table 1: Cold-Leg .txt File Structure**

Parameter	X (cm)	Y (cm)	Umean (m/s)	Vmean (m/s)	Usd (m/s)	Vsd (m/s)	Restress (m <sup>2</sup> /s <sup>2</sup> )
-----------	--------	--------	-------------	-------------	-----------	-----------	--

**Table 2: Downcomer .txt File Structure**

Parameter	Y (cm)	X (cm)	Vmean (m/s)	Umean (m/s)	Vsd (m/s)	Usd (m/s)	Restress (m <sup>2</sup> /s <sup>2</sup> )
-----------	--------	--------	-------------	-------------	-----------	-----------	--

“Umean” and “Vmean” are the time-averaged velocities.

“Restress” is the Reynolds Stress for the measurement duration.

The standard deviation was calculated using equation (1).

$$U_{sd} = \sqrt{\frac{1}{t-1} \sum_{i=1}^t |U_i - u|^2} \quad (1)$$

where t is the measurement duration, u is the mean of U,


$$\mu = \frac{1}{t} \sum_{i=1}^t U_i \quad (2)$$

The same method is applied to the standard deviation of the V component.

#### 4.1 Cold-Leg Data Sets

Data for the cold leg have been recorded for a period of time of 64.15 s. The experimental data are provided as time-averaged quantities calculated within a time interval of shown in Table 3. The first row of the table represents the data previously shared (Rev-0 of this document).

Time-averaged velocities, and Reynolds stresses were calculated based on the given time intervals for each measurement location (Table 3). File names are also listed on Table 3.

	TAMU Pressurized Thermal Shock Open Test Summary		
	Document No: TAMU-PTSUQ-OT3	Rev: 1.1	Page 11 of 13

**Table 3: Time-Averaged Intervals**

File Name	Start Time <sup>1</sup> (s)	End Time <sup>1</sup> (s)	Duration (s)	File Type
TAMU-PTSUQ-OT3-Rev-0-Cold_Leg	8.10	64.15	56.05	.txt
TAMU-PTSUQ-OT3-Rev-1-Cold_Leg_Set_1	6.38	16.38	10	.txt
TAMU-PTSUQ-OT3-Rev-1-Cold_Leg_Set_2	16.38	26.38	10	.txt
TAMU-PTSUQ-OT3-Rev-1-Cold_Leg_Set_3	26.38	36.38	10	.txt
TAMU-PTSUQ-OT3-Rev-1-Cold_Leg_Set_4	36.38	46.38	10	.txt
TAMU-PTSUQ-OT3-Rev-1-Cold_Leg_Set_5	46.38	56.38	10	.txt
TAMU-PTSUQ-OT3-Rev-1-Cold_Leg_Set_6	56.38	64.15	7.78	.txt


#### 4.2 Downcomer Data Sets

Data for the downcomer have been recorded for a period of time of 69.5 s. The experimental data are provided as time-averaged quantities calculated within a time interval of shown in Table 4. The first row of the table represents the data previously shared (Rev-0 of this document).

Time-averaged velocities, and Reynolds stresses were calculated based on the given time intervals for each measurement location (Table 4). File names are also listed on Table 4.

---

<sup>1</sup> All start and end times are taken with respect to the initial opening of the valve ( $t = 0 \text{ sec}$ ).


	TAMU Pressurized Thermal Shock Open Test Summary		
	Document No: TAMU-PTSUQ-OT3	Rev: 1.1	Page 12 of 13

**Table 4: Time-Averaged Intervals**

File Name	Start Time <sup>2</sup> (s)	End Time <sup>2</sup> (s)	Duration (s)	File Type
TAMU-PTSUQ-OT3-Rev-0-Downcomer	0	69.5	69.5	.txt
TAMU-PTSUQ-OT3-Rev-1.1-Downcomer	12.96	69.5	56.54	.txt
TAMU-PTSUQ-OT3-Rev-1-Downcomer_Set_1	10.84	20.84	10	.txt
TAMU-PTSUQ-OT3-Rev-1-Downcomer_Set_2	20.84	30.84	10	.txt
TAMU-PTSUQ-OT3-Rev-1-Downcomer_Set_3	30.84	40.84	10	.txt
TAMU-PTSUQ-OT3-Rev-1-Downcomer_Set_4	40.84	50.84	10	.txt
TAMU-PTSUQ-OT3-Rev-1-Downcomer_Set_5	50.84	60.84	10	.txt
TAMU-PTSUQ-OT3-Rev-1-Downcomer_Set_6	60.84	69.5	8.66	.txt

---

<sup>2</sup> All start and end times are taken with respect to the initial opening of the valve ( $t = 0 \text{ sec}$ ).

	TAMU Pressurized Thermal Shock Open Test Summary		
	Document No: TAMU-PTSUQ-OT3	Rev: 1.1	Page 13 of 13

## 5.0 ELECTRONIC ATTACHMENTS

The following files are included:

TAMU-PTSUQ-OT3-Rev-0-Cold\_Leg.txt  
 TAMU-PTSUQ-OT3-Rev-1-Cold\_Leg\_Set\_1.txt  
 TAMU-PTSUQ-OT3-Rev-1-Cold\_Leg\_Set\_2.txt  
 TAMU-PTSUQ-OT3-Rev-1-Cold\_Leg\_Set\_3.txt  
 TAMU-PTSUQ-OT3-Rev-1-Cold\_Leg\_Set\_4.txt  
 TAMU-PTSUQ-OT3-Rev-1-Cold\_Leg\_Set\_5.txt  
 TAMU-PTSUQ-OT3-Rev-1-Cold\_Leg\_Set\_6.txt

TAMU-PTSUQ-OT3-Rev-0-Dowcomer.txt  
 TAMU-PTSUQ-OT3-Rev-1.1-Downcomer.txt  
 TAMU-PTSUQ-OT3-Rev-1-Downcomer\_Set\_1.txt  
 TAMU-PTSUQ-OT3-Rev-1-Downcomer\_Set\_2.txt  
 TAMU-PTSUQ-OT3-Rev-1-Downcomer\_Set\_3.txt  
 TAMU-PTSUQ-OT3-Rev-1-Downcomer\_Set\_4.txt  
 TAMU-PTSUQ-OT3-Rev-1-Downcomer\_Set\_5.txt  
 TAMU-PTSUQ-OT3-Rev-1-Downcomer\_Set\_6.txt



APPENDIX E

TAMU-PTSUQ-BBC-001-REV2



## TECHNICAL DOCUMENT COVER PAGE

Document No:	TAMU-PTSUQ-BBC-001	Revision: 2	Page 1 of 10
		Date: 11/18/2018	
Doc Title:	Boundary Conditions –Blind Test		
Project Name:	Cold Leg Mixing CFD-UQ Benchmark		
Document Purpose/Summary:			
<p>This document provides a description of the boundary conditions, the parameters to be measured, and the measurement locations for the blind test.</p>			
<p>Total Page Count: 10 pages.</p>			



## TECHNICAL DOCUMENT COVER PAGE

Document No:	TAMU-PTSUQ-BBC-001	Revision: 2	Page 2 of 10
Doc Title:	Boundary Conditions – Blind Test		

Prepared by:	Daniel Orea
	Vasileios Kyriakopoulos
Reviewed by:	Rodolfo Vaghetto
	Thien Nguyen




Boundary Conditions – Blind Test

Document No: TAMU-PTSUQ-BBC-001

Rev: 2

Page 3 of 10

REVISION	DATE	DESCRIPTION
0	03/19/2018	First release
1	05/02/2018	Rev.1 Added list of parameters measured Added measurement locations Updated fluids' density with standard deviation
2	11/18/2018	Rev 2 Updated Figure 5.1 to identify locations of the origin of the coordinate systems

	Boundary Conditions – Blind Test		
	Document No: TAMU-PTSUQ-BBC-001	Rev: 2	Page 97 of 10


## TABLE OF CONTENTS

TABLE OF CONTENTS.....	97
DEFINITIONS AND ACRONYMS.....	98
1.0 SUMMARY AND SCOPE.....	99
2.0 WORKING FLUIDS SELECTION .....	99
3.0 BOUNDARY CONDITIONS.....	99
3.1 Density .....	99
3.1.1 Heavy Fluid Density.....	100
3.1.2 Light Fluid Density .....	100
3.1.3 Density Difference.....	100
3.2 Viscosity .....	100
3.2.1 Heavy Fluid Viscosity.....	100
3.2.2 Light Fluid Viscosity .....	100
4.0 INITIAL CONDITIONS.....	101
5.0 MEASUREMENTS AND LOCATIONS.....	102



## DEFINITIONS AND ACRONYMS

CL	Cold Leg
DC	Downcomer
DI	De-Ionized
H	Heavy
L	Light

	Boundary Conditions – Blind Test		
	Document No: TAMU-PTSUQ-BBC-001	Rev: 2	Page 6 of 10

## 1.0 SUMMARY AND SCOPE

This document is prepared to provide the boundary and initial conditions for the blind test, together with the parameter that will be measured during the tests, and their locations. These conditions are provided to the analysts to perform the simulations.

The following conditions are described in this document:

### Boundary Conditions

- Working Fluids' Density
- Working Fluids' Viscosity
- Density Difference

### Initial Conditions (Before Valve Opening)

- Heavy fluid liquid level

## 2.0 WORKING FLUIDS SELECTION

The following fluids are selected for the blind test:

### High Density Fluid

### Low Density Fluid


Fluid properties are described in Section 3.0 (Boundary Conditions)

## 3.0 BOUNDARY CONDITIONS

Density and viscosity of the selected working fluids are measured at the beginning of the blind test. The values reported in the following sections are targeted values.

### 3.1 Density

Densities are estimated by measuring the mass of a 10-ml sample taken from batch of solution maintained at a given temperature (Volume accuracy =  $\pm 0.055$  ml; Mass accuracy =  $\pm 0.0001$  g).

	Boundary Conditions – Blind Test		
	Document No: TAMU-PTSUQ-BBC-001	Rev: 2	Page 7 of 10

### 3.1.1 Heavy Fluid Density

The density of the heavy (H) fluid is:

$$\rho_H = 1107.07 \text{ kg/m}^3 \quad (\sigma_H = 6.505 \text{ kg/m}^3)$$

### 3.1.2 Light Fluid Density

The density of the light (L) fluid is:

$$\rho_L = 911.34 \text{ kg/m}^3 \quad (\sigma_L = 7.311 \text{ kg/m}^3)$$

### 3.1.3 Density Difference

The density difference achieved with the selected heavy and light fluids is:

$$\Delta\rho = \rho_H - \rho_L = 195.73 \text{ kg/m}^3$$

## 3.2 Viscosity

Viscosity is measured at 20.0 °C ±0.1 °C

### 3.2.1 Heavy Fluid Viscosity

The viscosity of heavy (H) fluid is:

$$\mu_H = 0.001377 \text{ Pa} \cdot \text{s} \pm 1.5\%$$

### 3.2.2 Light Fluid Viscosity

The viscosity of the light (L) fluid is:

$$\mu_L = 0.002867 \text{ Pa} \cdot \text{s} \pm 1.5\%$$





#### 4.0 INITIAL CONDITIONS

The initial conditions refer to the status of the liquid levels in the test facility at the time the test is initiated, which corresponds to the time the isolation valve is open.

When preparing the test, the light side of the facility will be filled with light fluid up to the top of the vessel as shown in Figure 4-1 (levels are referred to the cold leg centerline). The level of the light fluid correspond to the height of the reactor vessel (Figure 4-1, right), equal to:

$$H_L = 27.9 \text{ cm}$$

The level of the heavy fluid (Figure 4-1, left) is calculate from the densities of the fluids reported in Section 3.1, in order to equalize the pressure across the isolation valve at the test start.

$$H_H = \frac{\rho_L}{\rho_H} H_L = 22.97 \text{ cm}$$

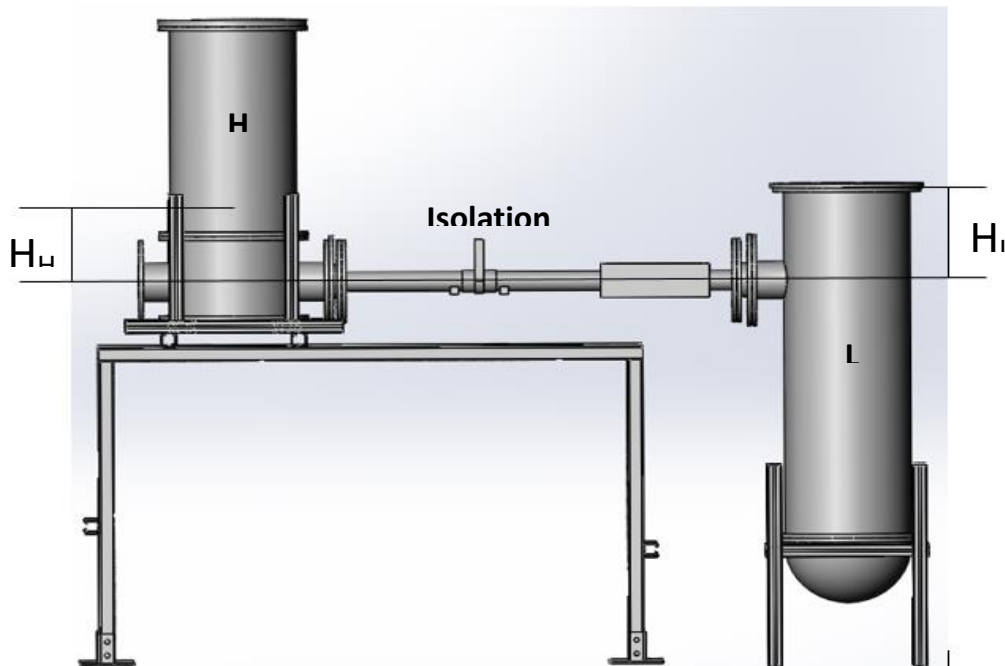



Figure 4-1. Liquid Levels

	Boundary Conditions – Blind Test		
	Document No: TAMU-PTSUQ-BBC-001	Rev: 2	Page 9 of 10

## 5.0 MEASUREMENTS AND LOCATIONS

The following experimental data will be included for the blind test. One *main line* and one *alternative line* are selected for the cold leg and downcomer. The measurement locations are shown in Figure 5-1. Coordinate systems for cold leg and downcomer measurements are also marked in Figure 5-1. The origin of the cold Leg measurements is located at the center of the isolation valve. The origin of the downcomer measurements is located at the intersection of the center-line of cold leg pipe and the center line of the downcomer annulus.

### COLD LEG

1. Time-averaged horizontal and vertical (U, V) velocity components along the main line CL1.
2. Time-averaged concentrations along the main line CL1.
3. Instantaneous horizontal and vertical velocity components at three selected points on the main line CL1.
4. Instantaneous concentrations at the three selected points on the main line CL1.
5. Time-averaged horizontal and vertical (U, V) velocity components along the alternative line CL2.
6. Time-averaged concentrations along the alternative line CL2.
7. Instantaneous horizontal and vertical velocity components at three selected points on the alternative line CL2.
8. Instantaneous concentrations at the three selected points on the alternative line CL2.

### DOWNCOMER

1. Time-averaged horizontal and vertical (U, V) velocity components along the main line DC1.
2. Time-averaged concentrations along the main line DC1.
3. Instantaneous horizontal and vertical velocity components at two selected points on the main line DC1.
4. Instantaneous concentrations at the two selected points on the main line DC1.
5. Time-averaged horizontal and vertical (U, V) velocity components along the alternative line DC2.
6. Time-averaged concentrations along the alternative line DC2.
7. Instantaneous horizontal and vertical velocity components at two selected points on the alternative line DC2.
8. Instantaneous concentrations at the two selected points on the alternative line DC2.



Boundary Conditions – Blind Test

Document No: TAMU-PTSUQ-BBC-001

Rev: 2

Page 10 of 10

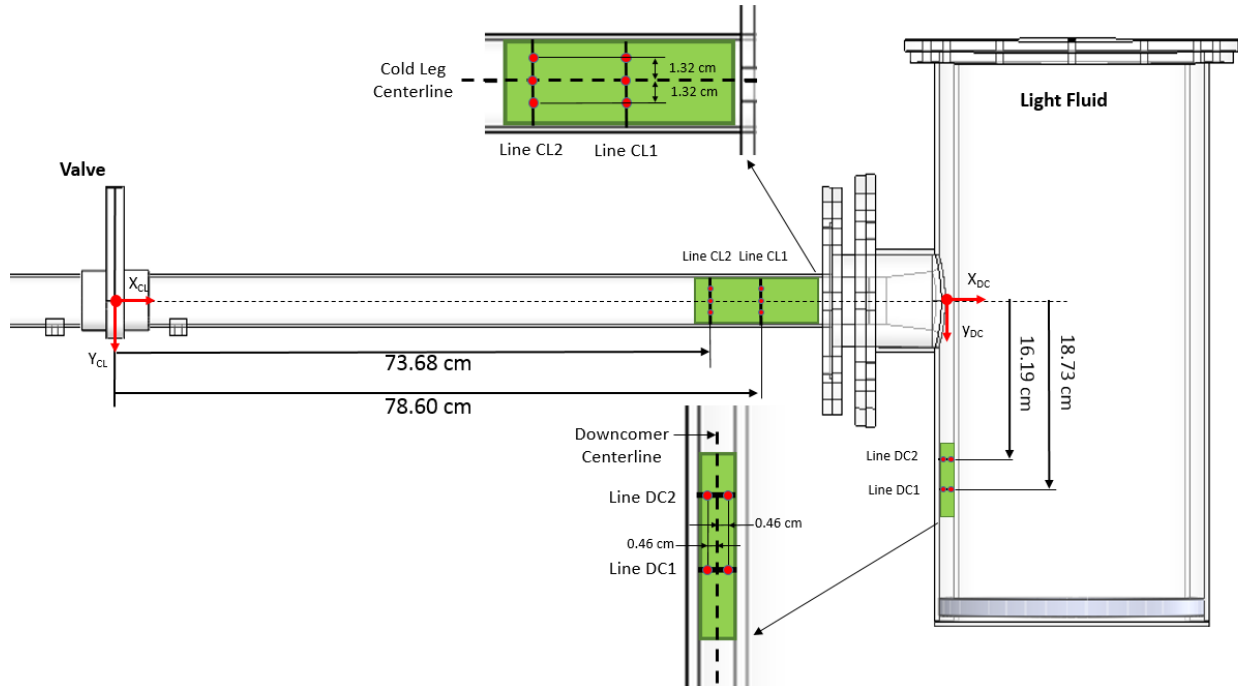


Figure 5-1. Measurement Locations